ESA Contract No. 4000139422/22/I-NS

Aeolus + Processes

Technical Note 2

Nedjeljka Žagar, Robin Pilch Kedzierski and Valentino Neduhal
Universität Hamburg

Giovanna de Chiara and Sean Healy
European Centre for Medium-Range Weather Forecasts

Hamburg and Reading, December, 2023, revised in April 2024

Aeolus + Processes, Technical Note 2
by Žagar et al.

Executive summary

The report presents results of the Work package 2 (WP2) of ESA Contract No. 4000139422/22/I-NS which focuses on Aeolus effects on the vertical momentum fluxes (VMFs) in the tropics. The VMFs are affected by Aeolus through changes in the horizontal winds and indirectly through vertical motions. The vertical velocity and VMFs are crucial variables to be realistically represented by high-resolution weather and climate models. In particular, the VMFs drive the stratospheric quasi-biennial oscillation (QBO) which experienced the second disruption on the record during the Aeolus operations.

The results show that the assimilation of Aeolus winds leads to a systematic, albeit small, reduction of the vertical velocity in the ECMWF system. It is related to the systematic reduction of the horizontal wind divergence reported in Technical Note 1. A significant impact of Aeolus in the kinetic energy spectra of vertical motions was found for the large-scale Kelvin waves with the strongest effect during the QBO disruption in early 2020.

During the QBO disruption, corrections of the background zonal wind in the lower stratosphere by Aeolus were particularly large. Changes in the analyses that increased the vertical shear of the zonal wind were aligned with changes in the VMFs. Average forecast improvements by Aeolus of a few % with respect to NoAEolus increased to about 15% improvements in day 1 forecasts in the lower stratosphere early in 2020 (see the figure). In normal QBO conditions such as summer 2020, Aeolus winds improved the transition from the easterly to westerly phase of the QBO. This shows as an alignment of wave forcing (i.e. the vertical gradient of the VMFs) with the changes in the background flow. In summer 2020, the forcing was largely due to the Kelvin wave and eastward-propagating inertia-gravity waves.

When measured by differences in zonally averaged fluxes within 10°S and 10°N, the effects of Aeolus winds on the VMFs are relatively small (below 1%). However, effects at individual scales can be large depending on the background flow and wave motions. In early 2020, the period of the QBO disruption, the assimilation of Aeolus winds in the ECMWF system resulted in up to about 20% change in stratospheric VMFs with respect to NoAeolus.

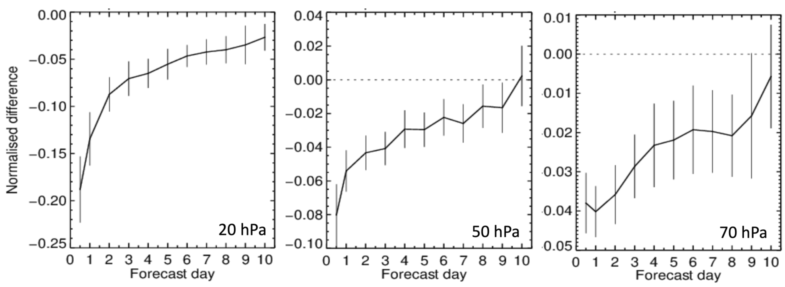

Normalized difference of the root-mean-square errors (rmse) of zonal wind forecasts at 70 hPa, 50 hPa and 20 hPa in the tropics in period 15 Feb-31 Mar 2020. The difference is taken between the rmse of Aeolus and NoAeolus experiments and the normalization is by the rmse of the NoAeolus experiment. Negative values of the normalized rmse mean improvement, and the error bars show 95% confidence intervals.

Contents

Chapter 1

Introduction

The ESA Contract No. 4000139422/22/I-NS, project ”Aeolus+Processes” investigates atmospheric processes and properties of the ECMWF prognostic system that were improved by the assimilation of Aeolus winds. In the ECMWF system, as well as in all other numerical weather prediction (NWP) systems which assimilated Aeolus winds, largest benefits were found in the tropics[2]. The results of the Work Package 1 (WP1) of the project, which was presented in Technical Note 1 (TN1), showed that the assimilation of Aeolus winds increased the vertical wind shear within the tropical upper troposphere and lower stratosphere (UTLS) in the ECMWF analyses, and increased the amplitudes of large-scale equatorial waves in the UTLS.

The follow-on Work Package 2 (WP2), which is presented in this TN, investigates the effects of the assimilation of Aeolus winds on the tropical middle atmosphere. The main objective of WP2 is to quantify the impact of the assimilation of Aeolus winds on the vertical momentum fluxes with a special attention to the 2019 disruption of the quasi-biennial oscillation (QBO). The QBO is the primary mode of variability in the lower tropical stratosphere (e.g. Baldwin et al., 2001). It is an oscillation in the zonal winds with a period that fluctuates between about 25 and 30 months. This is manifested as a downward propagation of easterly or westerly winds starting near the top of the lower stratosphere (near 10 hPa) and propagating downwards at about 1 km per month speed towards the tropopause. The driving mechanism of the QBO are waves emanating from the tropical troposphere including the Kelvin wave, mixed Rossby-gravity waves and a spectrum of inertia-gravity waves. The exact role of various waves in driving the QBO is not fully understood. Similarly, the role of the QBO on tropospheric processes and global predictability is a subject of intense research with QBO-associated teleconnections associated well documented in the tropics, subtropics and extratropics including practicaly all modes of variability (for example, the stratospheric polar vortex, the subtropical jets, the North Atlantic Oscillation, the Madden–Julian Oscillation). Despite its quasi-periodicity, large scale structure and importance, the QBO remains a major challenge for climate models (e.g. Richter et al., 2020, 2022).

[2]Collection of papers on the effects of Aeolus winds in global NWP models: `https://rmets.onlinelibrary.wiley.com/doi/toc/10.1002/(ISSN)1477-870X.aeolus`.

In order to simulate the QBO, weather and climate models need to accurately represent vertical motions associated with equatorial waves. Vertical motions are related to the horizontal winds observed by Aeolus through divergence; in essence, the vertical velocity at a level in the atmosphere is an integral of divergence in the atmospheric column above this level. By bringing changes to the horizontal motions, Aeolus can affect also updrafts and downdrafts. Vertical fluxes of the horizontal momentum can therefore be affected by Aeolus not only via changes in the horizontal winds but also through the vertical motions. This report quantifies these effects in the tropics using a two-year long Observing System Experiments (OSEs) with the ECMWF system.

In what follows, we first discuss scientific, practical and societal motivation for analysing if and how the assimilation of Aeolus winds affects the representation of the vertical velocity and associated vertical momentum fluxes in the ECMWF system. This is followed by specific goals of the WP2, their coupling to the recently completed WP1, and the report outline.

1.1 Vertical velocity and vertical momentum fluxes

The vertical velocity, w, is not an observed quantity of the global observing system (GOS). Sporadic observations of vertical velocity make evident the missing variance by the models, at least locally (e.g. Dörnbrack et al., 2018). Although the magnitude of vertical motions is on average much smaller than the magnitude of the horizontal wind velocity, it is a crucial ingredient of weather and climate models and a key variable to be realistically represented in km-scale models. For example, adiabatic cooling of rising air leads to condensation of water vapor and precipitation. Associated divergent circulation plays a key role in the dynamics of weather systems and related generation of relative vorticity. Vertical motions are a key ingredient in the conversion of potential to kinetic energy in the global atmosphere. Quantification of various components of general circulation, especially precipitation and water cycle requires a reliable estimate of vertical velocity.

Majority of global precipitation is within the tropical belt and is associated with strong updrafts within deep tropical convection. In the Northern hemisphere (NH) extra-tropics, the vertical velocity is most important for simulating precipitation in boreal winter in the storm-track regions of the Northern Atlantic and Pacific, and convective precipitation in boreal summer. With much of the global vertical velocity variance in the tropics, where the Aeolus impact has been the largest (Rennie et al., 2021), a question arises on effects of Aeolus horizontal line-of-sight (HLOS) winds on simulated vertical velocity and vertical momentum fluxes. This question is relevant for the ongoing DestinE project which aims at global simulations with km-scale horizontal grid and realistic representation of convection and precipitation, hence also the vertical velocity. The Aeolus follow-on missions will also benefit from a better understanding of the relationship between the HLOS winds and simulated vertical velocities and momentum fluxes in the ECMWF system.

The second Newton law for the vertical velocity $w = dz/dt$ per unit mass can be written as

$$\frac{\partial w}{\partial t} + u\frac{\partial w}{\partial x} + v\frac{\partial w}{\partial y} + w\frac{\partial w}{\partial z} = -\frac{1}{\rho}\frac{\partial p}{\partial z} - g + \frac{1}{\rho}\left(\frac{\partial \tau_{zx}}{\partial x} + \frac{\partial \tau_{zy}}{\partial y} + \frac{\partial \tau_{zz}}{\partial z}\right) + \nu\nabla^2 w \ . \tag{1.1}$$

Here, the terms of the left-hand side denote local (temporal) change of vertical velocity (first term) and changes due to advection by the three velocity components in the system with the vertical coordinate being height (other three terms). On the right-hand side of (1.1), the terms involving τ denote the stress on the large-scale flow exerted by the momentum flux of velocity fluctuations; for example, an average flux of x-momentum due to the small-scale motions across a surface z=constant is denoted $\overline{w'u'}$ and can be expressed as $\overline{w'u'} = -\tau_{xz}/\rho$. The first term on the right-hand side is the vertical component of the pressure gradient force, the second term is the gravity and the last term represents flow viscosity. We also note that Eq. (1.1) on the spherical Earth includes the vertical component of the Coriolis force and a curvature term.

Dynamical cores of several global numerical weather prediction models, including the ECMWF model, are hydrostatic. Under the hydrostatic balance approximation, Eq. (1.1) is replaced with the two largest terms on its right-hand side, i.e.

$$\partial p = -\rho g \partial z \ .$$

The vertical velocity is a diagnostic quantity usually derived from the mass continuity equation. The effects of other terms in Eq. (1.1), especially the vertical momentum fluxes, have to be parameterised. The same applies to the momentum fluxes in the prognostic equations for horizontal motions.

Day-to-day weather analysis and interpretation is in practice performed in the system which has pressure as the vertical coordinate, with w replaced by the pressure vertical velocity omega, $\omega = dp/dt$. Same applies for majority of climate research. In the ECMWF system, the pressure vertical velocity is diagnosed on model levels and then interpolated on pressure levels (Simmons and Burridge, 1981). The ω fields from reanalyses validate the present-day climate simulated by climate models in support of modelling of climate futures.

If the vertical motion is poorly observed, how can it be understood with the help of the horizontal HLOS winds? Across many scales and processes, significant vertical velocities are signatures of wave motions, primarily internal gravity waves (e.g. Nappo, 2002) that are generated by processes such as interaction of the flow with orography, surface and boundary layer processes, tropospheric moist convection, frontogenesis, imbalances of synoptic jets and wave-wave interactions (e.g. Fritts and Alexander, 2003). As waves propagate vertically, they break, dissipate and deposit momentum to the zonal mean flow. Small-scale gravity waves together with the large-scale Kelvin and mixed Rossby-gravity drive the QBO in the lower tropical stratosphere. The small horizontal scales and short periods of the waves represent a challenge for NWP models, even at km scale. The wave effects are therefore parameterized (Plougonven et al., 2020). Effects of parameterized wave forcing of the zonal mean flow are diagnosed using the transformed Eulerian-mean momentum budget (Andrews et al., 1987). The diagnostic involves the evaluation of the vertical flux of the horizontal momentum associated with waves, $\overline{w'u'}$ and $\overline{w'v'}$. Here, the overbars denote zonal averaging and the primes denote deviations of the zonal mean of the fields u, v and w.

With demonstrated Aeolus effects on large-scale equatorial waves and the importance of the vertical velocity and VMFs in the NWP and climate models, it is relevant to understand the influence of the assimilation of the horizontal-line-of sight (HLOS) winds on the two quantities. This argument motivated the implementation of VENUS, the Aeolus range bin setting optimized for the tropical upper troposphere and lower stratosphere in April 2020.

1.2 Motivation and goals of Work Package 2

In WP2, we investigate whether and how an improved representation of the tropical horizontal circulation, reported in TN1, leads also to changes in the vertical velocity and VMFs in the ECMWF system. Similar to WP1, the initial focus is on the tropical upper troposphere where vertically-propagating waves that drive variability in the tropical stratosphere are excited.

The Aeolus effects in the UTLS and above depend on the flow, in particular on the state of the QBO. It is important to establish coupling between Aeolus HLOS winds and the QBO because the QBO provides a predictability source for the extratropical circulation on seasonal and longer time scales (e.g. Scaife et al., 2014). In recent years, two disruptions of the QBO took place for the first time since the beginning of the QBO regular detection in 1953, and the second disruption was observed by Aeolus (Banyard et al., 2024). Anstey et al. (2021) suggested, based on their analysis of climate model projections, that disruptions to the QBO are likely to become more common in the future implying that the QBO may become a less reliable source of predictability. In line with this argument, Raphaldini et al. (2020) argued, based on the ERA-Interim reanalysis data, that a large-scale regime transition has already taken place in the recent decades.

A key question associated with the QBO dynamics is the zonal wavenumber spectrum and relative roles of various waves driving the QBO. In particular, how different was the wave forcing during the disruption from usual QBO evolution? What was the impact of Aeolus winds on the VMFs in the UTLS region during the 2019 QBO disruption? This question goes well beyond the present Aeolus impact and should lead to an improved understanding of the potential impact of future spaceborne Doppler wind lidars on middle atmosphere processes in a changing climate.

The WP1 presented evidence of enhanced amplitudes of large-scale equatorial waves and stronger wind shear in the UTLS. Based on this, we expect some effects of Aeolus winds on the vertical velocity and VMFs in the ECMWF system, although they may also reflect biases in other components of the GOS, data assimilation properties or model shortcomings. If the combined effect is positive and dominated by benefits of the Aeolus wind assimilation, it should be seen in improvements in stratospheric forecasts during periods with enhanced wave activity such as the QBO disruption. Therefore, the WP2 analyzed the effects of the Aeolus wind assimilation focusing on the evaluations of

1. scale-dependent effects on the vertical velocity in the UTLS,
2. scale-dependent effects on the vertical momentum fluxes, and
3. flow-dependent effects on the vertical momentum fluxes and stratospheric forecasts.

1.3 Outline of the report

In order to carry out the three tasks, a methodology is needed that filters the horizontal and vertical velocity perturbations associated with wave flows in the tropics. The method is summarized in Chapter 2 and the reader is referred to scientific papers for details. The input data is the same as in WP1 which is presented in details in De Chiara et al. (2023).

Results are organized in three chapters. Chapter 3 discusses effects of Aeolus data on vertical motions whereas Section 4 presents analysis of the vertical momentum fluxes. Both chapters present two complementary views, wave space analysis and analysis in physical space. Section 5 provides coupling between the presented results and the evolution of forecast quality in the stratosphere.

Finally, summary and conclusions highlight importance of various aspects of the presented work for follow-on work packages 4 and 5 and for Aeolus follow-on missions.

Chapter 2

Methodology

Similar to Technical Note 1, we apply the wave decomposition software MODES (Žagar et al., 2015) for filtering of the horizontal velocity perturbations associated with the equatorial waves and their scales. The tropical circulation is represented in terms of the Rossby and non-Rossby waves, superimposed on the zonal mean state. The non-Rossby wave species are made of the Kelvin waves, the mixed Rossby-gravity (MRG) waves and the inertia-gravity (IG) waves which consist of the eastward-propagation (EIG) and westward-propagation (WIG) waves. These five wave species span wave space to be discussed in this report. The vertical velocity filtering relies on a novel method derived from the same physical framework as MODES (Žagar et al., 2023) whereas the associated method for the computation of the VMFs has been implemented within the PhD project of V. Neduhal.

2.1 Decomposition of the horizontal and vertical velocities

Each wave specie has its u, v and ω velocity perturbation field. For example, the total zonal wind signal u at pressure level p, latitude φ and longitude λ is the sum of the zonal mean zonal wind u_0 and perturbations associated with the Rossby (R), EIG (E), WIG (W), Kelvin (K) and MRG (M) wave species, denoted by primes:

$$\begin{aligned} u(\lambda,\varphi,p) &= u_0(\varphi,p) + u'(\lambda,\varphi,p) \\ &= u_0(\varphi,p) + u'_K(\lambda,\varphi,p) + u'_M(\lambda,\varphi,p) + u'_E(\lambda,\varphi,p) + u'_W(\lambda,\varphi,p) + u'_R(\lambda,\varphi,p)\,. \end{aligned} \tag{2.1}$$

The same applies to the pressure vertical velocity ω:

$$\begin{aligned} \omega(\lambda,\varphi,p) &= \omega_0(\varphi,p) + \omega'(\lambda,\varphi,p) \\ &= \omega_0(\varphi,p) + \omega'_K(\lambda,\varphi,p) + \omega'_M(\lambda,\varphi,p) + \omega'_E(\lambda,\varphi,p) + \omega'_W(\lambda,\varphi,p) + \omega'_R(\lambda,\varphi,p)\,. \end{aligned} \tag{2.2}$$

The zonal mean zonal wind u_0 is almost entirely made of the Rossby modes whereas ω_0 is normally zero.

In wave space, velocity components u and ω are represented using the Hough harmonics expansion which replaces latitudinal dependence by the zonal wavenumber k. Using the spectral Hough expansion coefficients produced by the application of MODES to the full 3D dataset, the zonal wind expansion along the altitude circle is

$$u\,(\lambda,\varphi,p) = \sum_{m=1}^{M} \sqrt{gD_m} \sum_{n=1}^{R} \sum_{k=-K}^{K} \chi_n^k\, U_n^k\,(\varphi;m)\,\mathrm{e}^{\mathrm{i}k\lambda} G_m(p)\,, \tag{2.3}$$

so that the expansion expansion coefficients in the Fourier series representation are defined as

$$\begin{aligned}\hat{u}_k(\varphi,p) &= \sum_{m=1}^{M} \sqrt{gD_m} \sum_{n=1}^{R} \chi_n^k(m) U_n^k\,(\varphi;m)\, G_m(p) \quad \text{with} \quad u(\lambda,\varphi,p) \\ &= \sum_{k=-K}^{K} \hat{u}_k(\varphi,p) e^{\mathrm{i}k\lambda}\,.\end{aligned} \tag{2.4}$$

In the expansion (2.3), the spectral expansion coefficients of 3D data is denoted $\chi_n^k(m)$ and it is defined by the meridional and vertical mode indices n and m, respectively in addition to k. The summation over the n and m accounts for contributions of all vertical structure functions $G_m(p)$ at level p, and the meridional Hough functions for the zonal wind $U_n^k\,(\varphi;m)$. The summation over n takes into account five wave species listed above, their sum equal R. The number of vertical modes M is defined by the number of vertical levels and chosen truncation. For every vertical mode m, the parameter D_m represents the coupling between the vertical and horizontal structures, and it is known as the "equivalent depth". The number of waves along the latitude circle is K. The zonal wavenumber $k = 0$ corresponds to the zonal mean zonal wind u_0 in (2.1). Further details of the applied flow decomposition can be found in Žagar and Tribbia (2020) and Žagar et al. (2015).

For the vertical velocity, the expansion along the latitude circle is

$$\omega\,(\lambda,\varphi,p) = \sum_{k=-K}^{K} \hat{\omega}_k\,(\varphi,p)\,\mathrm{e}^{\mathrm{i}k\lambda}\,, \tag{2.5}$$

with

$$\hat{\omega}_k\,(\varphi,p) = -\sum_{m=1}^{M} \sum_{n=1}^{R} \mathrm{i}\nu_n^k(m)\chi_n^k(m) Z_n^k\,(\varphi;m) \int_0^p G_m(p')\mathrm{d}p'\,. \tag{2.6}$$

Here, Z_n^k is the Hough function for the geopotential height, ν is the eigen frequency for the mode (k,n,m) and the imaginary unit $\mathrm{i} = \sqrt{-1}$. The derivation of (2.6) can be found in **?**.

Similar to physical space, the zonal wavenumber space representation of u and ω is additive, meaning that

$$\hat{u}_k\,(\varphi,p) = \hat{u}_0 + \hat{u}_K + \hat{u}_M + \hat{u}_E + \hat{u}_W + \hat{u}_R\,, \quad \text{and} \tag{2.7a}$$

$$\hat{\omega}_k\,(\varphi,p) = \hat{\omega}_0 + \hat{\omega}_K + \hat{\omega}_M + \hat{\omega}_E + \hat{\omega}_W + \hat{\omega}_R\,. \tag{2.7b}$$

The zonal wavenumber spectrum of the kinetic energy of vertical motions, the vertical kinetic energy (VKE) spectrum, is

$$E_V^k(\varphi,p) = (1-\delta_{k0})\,|\hat{\omega}_k|^2\,, \tag{2.8}$$

where $\delta_{k0} = 1/2$ for $k = 0$ and 0 otherwise (with $\hat{\omega_k}$ presented only for positive k). Using the Parseval theorem, the VKE per unit mass integrated around a latitude circle, E_V, is equal to the sum of its components in all zonal wavenumbers plus the zonal mean state:

$$E_V(\varphi, p) = \frac{1}{L}\int_0^L \frac{\omega^2}{2}\mathrm{d}x = \sum_{k=-K}^{K} \frac{|\hat{\omega}_k|^2}{2} = \sum_{k=0}^{K} E_V^k\,, \tag{2.9}$$

where $L = 2\pi a \cos\varphi$ is the circumference at latitude φ and $\mathrm{d}x = a\cos\varphi\,\mathrm{d}\lambda$. Limiting the summation (2.9) to the Rossby or non-Rossby (or IG) modes gives their individual VKE spectra.

2.2 Computation of the vertical momentum fluxes

Each of the five wave components in (2.1) and (2.2) contributes to the vertical momentum flux $\omega' u'$, meaning that $\omega' u'$ is made of 25 components, as illustrated in Table 1. Rows in the table represent the zonal wind perturbations due to the Rossby (R), EIG (E), WIG (W), Kelvin (K) and MRG (M) waves, whereas columns account for five components of vertical velocity perturbations. The summation of the elements in the first column thus provides the vertical flux of the zonal momentum associated with the Kelvin waves. Similarly, the last column is the vertical flux of the zonal wind perturbations associated with the Rossby waves. Table 1 is written for physical space, with perturbations defined as differences between the total signal and its zonal mean. An equivalent table can be made for wave space, with a single table for a single zonal wavenumber and table elements made of wave component k for each wave specie. A table for $\omega' v'$ is prepared in the same way.

The fact that 25 components of the zonal momentum flux are additive provides a scale-dependent evaluation of VMFs that is a novelty of our analysis. Namely, a typical approach to the computation of VMFs involves the truncation of model fields in space of spherical harmonics so that all fields with wavenumbers greater than a truncation number are assigned to gravity waves. A typical truncation scale in the ECMWF system is the global wavenumber 20 (e.g. Polichtchouk et al., 2022) which corresponds to the horizontal

Table 2.1: Components of the vertical flux of the zonal wave momentum, $\omega' u'$. Both ω' and u' are a linear combination of the five wave species: the Rossby (R), EIG (E), WIG (W), Kelvin (K) and MRG (M) waves.

$\omega' u'$	Kelvin	MRG	EIG	WIG	Rossby
Kelvin	$\omega'_K u'_K$	$\omega'_K u'_M$	$\omega'_K u'_E$	$\omega'_K u'_W$	$\omega'_K u'_R$
MRG	$\omega'_M u'_K$	$\omega'_M u'_M$	$\omega'_M u'_E$	$\omega'_M u'_W$	$\omega'_M u'_R$
EIG	$\omega'_E u'_K$	$\omega'_E u'_M$	$\omega'_E u'_E$	$\omega'_E u'_W$	$\omega'_E u'_R$
WIG	$\omega'_W u'_K$	$\omega'_W u'_M$	$\omega'_W u'_E$	$\omega'_W u'_W$	$\omega'_W u'_R$
Rossby	$\omega'_R u'_K$	$\omega'_R u'_M$	$\omega'_R u'_E$	$\omega'_R u'_W$	$\omega'_R u'_R$
	$\omega' u'_K$	$\omega' u'_M$	$\omega' u'_E$	$\omega' u'_W$	$\omega' u'_R$

wavelength of about 2000 km at the equator. All longer scales represent large-scale waves and they are a mixture of the Rossby, Kelvin and MRG signals, but also lagre-scale IG modes. Another filtering approach is to carry out wavenumber-frequency filtering and to assign a certain region of wavenumber-frequency space to a single wave specie (e.g. Kim and Chun, 2015a). In contrast, our unified decomposition of the vertical momentum fluxes allows coexistence of different wave species in the same frequency and wavenumber bands.

We can define the vector of the vertical transfer of the horizontal momentum in physical space as

$$\boldsymbol{F}(\lambda, \varphi, p) = (F_u, F_v) = (\omega' u', \omega' v') \ . \tag{2.10}$$

Physical interpretation of $\boldsymbol{F}$ is not simple and it is is not helped by its unit of Pascal meter second^{-2}. It can be simplified by using the approximation $\omega \approx -\rho g w$ which couples vertical velocities in the pressure and height systems in the hydrostatic atmosphere. Evaluating $-\left(\omega' u', \omega' v'\right)/g$ provides VMFs in units of Pascal and coupled with the height system VMFs $(\rho w' u', \rho w' v')$. This is the approach followed in most of studies of VMFs. For the sake of comparison with published studies, we will thus present VMFs as

$$\boldsymbol{F}(\lambda, \varphi, p) = (F_u, F_v) = \left(-\frac{1}{g}\overline{\omega' u'}, -\frac{1}{g}\overline{\omega' v'}\right) \ , \tag{2.11}$$

where the overbar defines averaging in space and time, with details explained in the result sections.

Substituting u, v and ω with their modal expansion series, and using the orthogonality properties of the expansion functions, the complex cross-spectrum of the VMFs can be expressed as

$$\hat{\boldsymbol{F}}_k(\varphi, p) = (F_{k,u}, F_{k,v}) = \left(\hat{\omega}_k[\hat{u}_k]^*, \hat{\omega}_k[\hat{v}_k]^*\right) , \tag{2.12}$$

where k takes both positive and negative values. In practice, only $k \geq 0$ is needed so that all $k > 0$ elements are mutliplied by a factor of 2. Each component of $\hat{\boldsymbol{F}}_k(\varphi, p)$ is multiplied by $-1/g$ to make the spectral and physical space analysis consistent. The discussed zonal wavenumber spectra of the VMFs thus correspond to

$$\hat{\boldsymbol{F}}_k(\varphi, p) = (F_{k,u}, F_{k,v}) = \left(-\frac{1}{g}\overline{\hat{\omega}_k[\hat{u}_k]^*}, -\frac{1}{g}\overline{\hat{\omega}_k[\hat{v}_k]^*}\right) , \tag{2.13}$$

with overline representing latitudinal and temporal averaging.

The real part of the cross-spectrum, $\Re(\hat{\boldsymbol{F}}_k)$, is the co-spectrum (or spectrum) of VMFs while the imaginary part, $\Im(\hat{\boldsymbol{F}}_k)$ is the quadrature spectrum of VMFs. The zonal wavenumber power spectrum of VMFs satisfies the Parseval theorem

$$\frac{1}{2\pi}\int_0^{2\pi} \boldsymbol{F} \mathrm{d}\lambda = \sum_{k=1}^{K} \Re(\hat{\boldsymbol{F}}_k) \, . \tag{2.14}$$

The co-spectrum describes a part of the u and ω and v and ω signals that are in phase. The quadrature spectrum describes the out-of-phase part of the u and ω and v and ω signals.

2.3 Observing System Experiment (OSE)

The WP2 relies on the outputs of WP1. Its input are analysis data from the FM-B second reprocessing OSE between July 2019 and June 2021. This longest running OSE was produced within the ESA-funded project on effects of Aeolus winds on extreme weather. Technical and other aspects of the observing system experiment have been presented by De Chiara et al. (2023).

The experiment which included Aeolus winds on top of all other observations (exp 'hls0' in MARS) is denoted "Aeolus". The reference experiment with all observations except Aeolus (exp 'hlpv' in MARS) will be referred to as "NoAeolus". The 2-year long period with analyses at 00 and 12 UTC were decomposed in WP1 by the wave-decomposition software MODES installed at the ECMWF Bologna computer. Results focuses on the effects of Aeolus winds in the ECMWF system by taking differences between the "Aeolus" and "NoAeolus" experiments, normalized by the "NoAeolus" experiment when needed to quantify the impact.

In agreement with previous reports by Rennie et al. (2021) and Rennie and Isaksen (2024), the largest analysis increments in the ECMWF system by assimilating Aeolus winds are in the tropical UTLS region and concretely in the tropical zonal wind in the layer 200-100 hPa. This is the layer right below the tropical tropopause where waves generated by convection, wave-mean flow and wave-wave interactions propagate upward and meet the descending lines of the QBO.

In the WP1 report, we presented evidence that the assimilation of Aeolus winds increases the vertical wind shear within the UTLS in the ECMWF system. The positive effect was found to be the strongest in $100 - 180$ hPa layer. Systematic effects of the assimilation of Aeolus winds were found in the divergent circulation projecting onto the WIG and EIG modes with Aeolus systematically attempting to reduce the amplitude of EIG and WIG modes in the tropics.

Technical work for WP2 included the computation of the vertical velocity associated with the main equatorial wave types in physical space and the computation of the spectral components of vertical velocity by (2.5). Similar computations were carried out for the zonal and meridional velocity components. This was followed by the computation of the wave components of VMFs defined by (2.13). The VMFs defined by (2.11) are computed in physical space involving combinations of u, v and ω components. Relevant results are presented in next two chapters. A time-dependent evaluation of the root-mean-square errors of the 10-day forecasts generated by the "Aeolus" and "NoAeolus" experiments is presented in Chapter 5.

Chapter 3

Effects of Aeolus winds on vertical motions in the tropics

This chapter presents the effects of Aeolus winds on the vertical velocity in the UTLS during the OSE period and paying special attention to the QBO disruption. First we present scale-dependent features of the vertical velocity spectrum in the tropics, using the framework recently developed by Žagar et al. (2023). Scale analysis shows zonal scales affected by the assimilation of the HLOS winds. This is followed by a detailed discussion of the vertical velocity in physical space, beginning with the description of the method for constructing vertical velocity composites. The method is similar to that used to summarize Aeolus effects on the horizontal motions in WP1, described in TN1. The quantification of Aeolus effects on the vertical velocity establishes whether effects on VMFs, discussed in the following chapter, result only from the changes in the horizontal winds or also from the changes in vertical motions.

3.1 Scale-dependent effects

A large intermittency in vertical motions in space and time makes the evaluation of differences in vertical velocity between Aeolus and NoAeolus experiments difficult. Using quadratic quantities such as the VKE and squared differences in vertical velocity can highlight scales and wave species with vertical velocity most affected by the assimilation of Aeolus winds. For this purpose, this section discusses time averaged differences in the VKE and time averaged squared differences (or mean-square difference, MSD) in omega. The VKE was defined in Chapter 2 (Eq. 2.8), whereas the MSD at zonal wavenumber k is computed as

$$MSD^k_\omega(\varphi, p) = \frac{1}{N-1}\sum_{t=1}^{N}\left(\omega^k_A(t) - \omega^k_{nA}(t)\right)\left(\omega^k_A(t) - \omega^k_{nA}(t)\right)^* \ , \tag{3.1}$$

where A and nA denote the Aeolus and NoAeolus experiment, respectively, $*$ is the complex conjugate operator, and the summation is over N samples. If we use $\Delta\omega^k$ to denote the difference, $\Delta\omega^k(t) = \omega^k_A(t) - \omega^k_{nA}(t)$, then the time-averaged $\Delta\omega^k$ should be zero if the effects of Aeolus assimilation on the vertical velocity are random, i.e. there is no systematic changes due to Aeolus. This is evaluated by amplitudes of the time-averaged differences, or the squared mean difference, denoted MD2, defined as

$$MD2^k_\omega(\varphi, p) = \overline{\Delta\omega^k}\left(\overline{\Delta\omega^k}\right)^* \ , \tag{3.2}$$

where overline denotes time averaging. In the computation of the average VKE differences and MSD, averaging is applied either to bi-monthly data or to the complete study period.

3.1.1 Spectra of the vertical kinetic energy in the NoAeolus experiment

Before discussing differences, we show in Fig. 3.1 the zonal wavenumber spectra of VKE for the NoAeolus experiment averaged for the 12 UTC analysis over the 2-year period. Time-averaged spectra for Aeolus experiment look almost identical in such a figure which spans multiple orders of magnitude as the VKE is per unit mass, or in units of Jkg^{-1}. The purpose of Fig. 3.1 is to show average properties of the VKE spectra associated with various wave type. It demonstrates that majority of the VKE is associated with IG waves as could be expected given that the vertical velocity is vertically integrated divergence of the horizontal wind. However, Kelvin wave VKE in the UTLS region can be comparable in amplitude at large and synoptic scales. This feature is of relevance for Aeolus which systematically corrects Kelvin wave signals. Note that y-axis is different among the panels: Total, non-Rossby and IG VKE have the same scale, the Rossby and MRG VKE use the same scale different from IG VKE, and the Kelvin VKE has another scale. The total VKE spectrum is significantly more shallow compared to the horizontal kinetic energy spectra. As discussed in Žagar et al. (2023), ideally the VKE IG spectrum should follow a 1/3 power law in the inertial range. The IFS model thus lacks vertical motions at subsynoptic scales.

The spectra in Fig. 3.1 are smoother than the VKE spectra in Fig. 3.2 as the former are averaged over around 10 model levels within various layers. But we show here Fig. 3.2 as differences between the Aeolus and NoAeolus will be presented without vertical averaging.

3.1.2 Differences between Aeolus and NoAeolus experiments

Aeolus effects on the vertical velocity can be seen across all scales as shown in Fig. 3.3 and Fig. 3.4. But, the effects are small. Figure 3.3 presents the MSD spectra (Eq. 3.1) for the total signal and its IG and Kelvin wave components whereas Fig. 3.4 presents the same three components for the MD2 (Eq. (3.2).

The two figures demonstrate that Aeolus, by changing the horizontal motions as discussed in TN1, is also affecting the divergence field, and thereby vertical velocity. Systematic changes (Fig. 3.4) can be quantified by comparing the amplitudes of MD2 and VKE, and will be carried out also in physical space. However, a two-order difference between MSD and VKE at large and synoptic scales (k¡15 corresponds to scales greater than about 1300 km) means that the effects are below 1% of the vertical velocity variance field. The MSD and MD2 both increase in magnitude with height, as does the VKE, because they all present variance per unit mass.

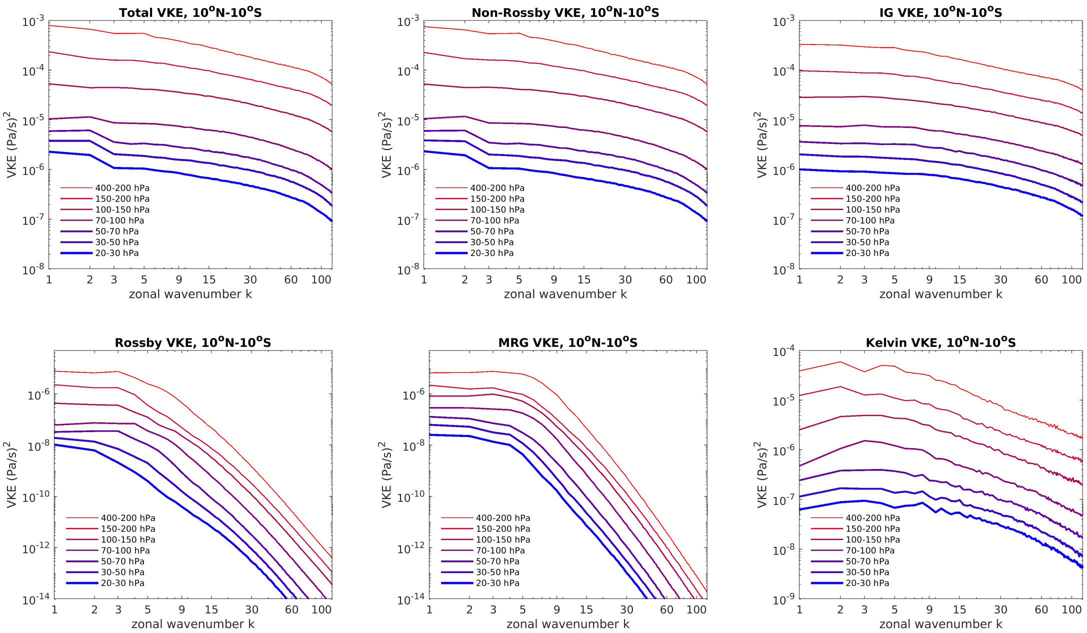

Figure 3.1: Zonal wavenumber spectra of the kinetic energy of vertical motions (VKE) per unit mass in the NoAeolus experiment averaged for the tropical belt between 10^{o}N and 10^{o}S and period July 2019 to June 2021. The bottom spectrum (thick blue line) in each panel is the average over levels between 20 and 30 hPa, and the spectra above belong to layers lower in the atmosphere as defined in the legend.

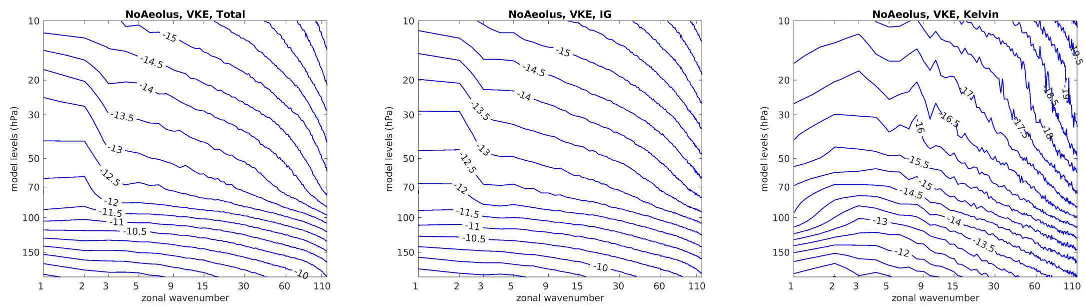

Figure 3.2: As in Fig. 3.1, but logarithm of the VKE as a function of the zonal wavenumber and vertical pressure level. The x- and y axis use the logarithmic scale.

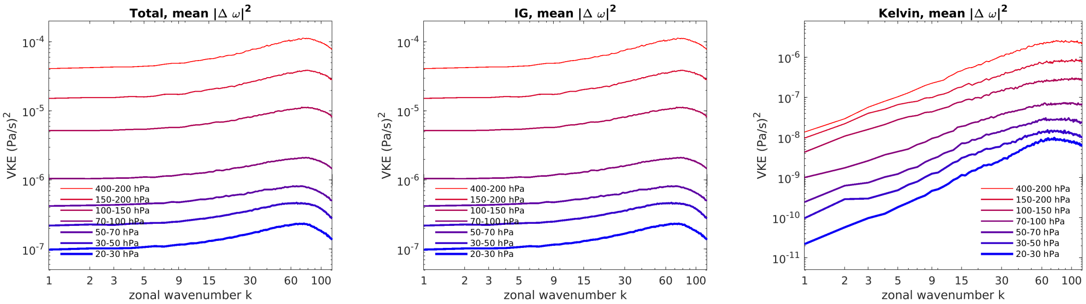

Figure 3.3: Mean squared vertical velocity differences (MSD) between the Aeolus and NoAeolus experiments. Averaging is carried out for the complete period July 2019 and June 2021, for latitudes between 10^{o}N and 10^{o}S and for multiple vertical levels as denoted in the legend.

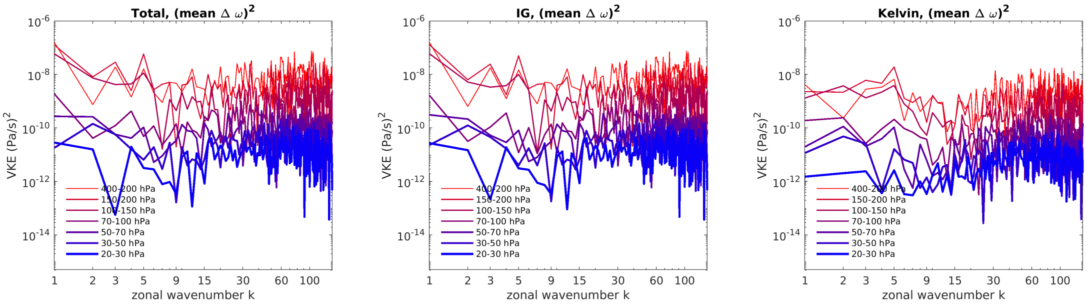

Figure 3.4: As in Fig. 3.3, but the squared mean difference (MD2).

The MSD spectra suggests that Aeolus effects on the vertical velocity depend on the zonal scale and are greater at smaller scales, especially for the Kelvin waves (Fig. 3.3). A peak difference near $k \approx 80$ remains to be explained and may be related to the model numerics. Overall, the MSD spectra demonstrate the fact that the spectral distribution of the horizontal wind divergence in the tropics depends on the wave type as elaborated in Neduhal et al. (2023). Although differences have small amplitudes, their spectral distribution may be useful for understanding the use of HLOS observations in the 4D-Var assimilation system and will be further investigated in WP5 of the project. The MD2 spectra appear noisy, show no significant scale dependence and are overall very small, i.e. multiple orders of magnitude smaller than MSD. Nevertheless, for the sake of results in physical space, we note that the signal itself i.e. VKE spectra falls off much faster than differences i.e. the MSD and MD2 spectra suggesting that effects grow relatively larger as the scale decreases.

Time averaged VKE differences normalized by the NoAeolus VKE (Fig. 3.5) suggest that Aeolus effects are well below 1% at large and synoptic scales except for the Kelvin wave, and that effect too noisy to interpret at subsynoptic scales, despite averaging over 2 years of data. The only large-scale wave signal significantly affected by Aeolus is the Kelvin wave which is thus shown in more details in Fig. 3.6. The 2-year averaged VKE difference is up to 4% at $k = 3-5$ in the tropical tropopause layer (Fig. 3.5,right). Most of the signal comes from the first study year and especially the period associated with QBO disruption. This can be seen in Fig. 3.6a,b in the VKE difference averaged for Nov-Dec

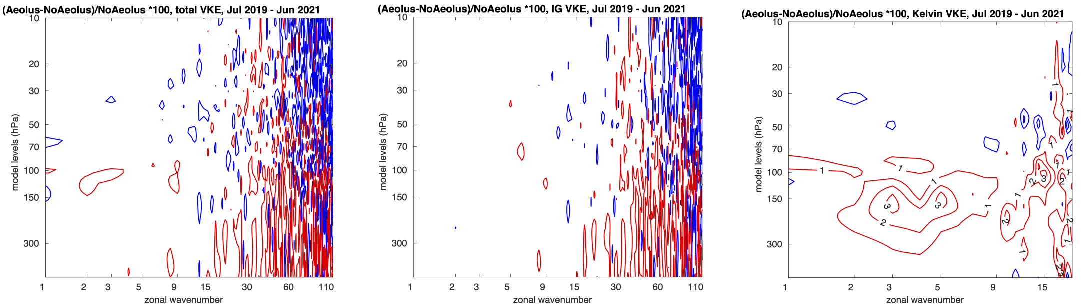

Figure 3.5: Differences in the VKE between the Aeolus and NoAeolus experiments normalized by the NoAeolus VKE. Averaging is performed between 10^oN and 10^oS and for 2 months at time. Left: All modes, Middle: IG modes, Right: Kelvin waves only for $k < 20$. Contouring for all modes and IG modes is ± 1, ± 3, ± 6, ± 15, etc, whereas for the Kelvin modes the contouring is every ± 1 till ± 6, then ± 8, etc. Averaging is carried out for the complete period July 2019 and June 2021, for latitudes between 10^oN and 10^oS and for multiple vertical levels as denoted in the legend.

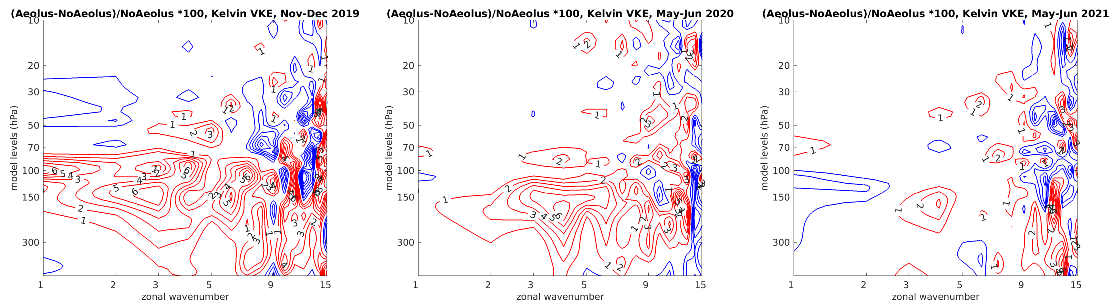

Figure 3.6: As in Fig. 3.5 for the Kelvin wawes, but for (left) Nov-Dec 2019, (middle) May-June 2020 and (right) May-June 2021.

2019 and May-June 2020. In contrast, there is little VKE difference in May-June 2021 (Fig. 3.6c). The positive sign of the average difference indicates that Aeolus intensifies the vertical velocity in Kelvin waves in the TTL layer. As they normally propagate vertically, we hypothesize that stratospheric forecasts, which depend on the wave forcing from the UTLS, will also manifest temporal variability with regard effects of Aeolus. This will be investigated in Chapter 5.

3.2 Effects in physical space

The magnitude range of vertical velocity significantly varies with altitude due to its unit Pa/s. To include both the troposphere and the stratosphere in the same plot, ω-composites are presented using an x-axis normalized by the standard deviation of ω at the same level. This is different from the compositing method for the zonal wind differences in TN1, which were presented with respect to the zonal wind itself. For each pressure level, the standard deviation of ω, σ_ω, is calculated for the NoAeolus experiment. Differences in ω are normalized by each level's pressure, thus having s^{-1} units and being proportional to the vertical velocity in altitude coordinates (but without the length scale). Binning is performed every 0.25 σ_ω, i.e. relative to the distribution range of ω at that level, not to the ω magnitude itself.

The interpretation of omega is not changed, and it is summarized in Table 3.1. When the sign of the vertical velocity in the NoAeolus experiment is negative ($\omega_{nA} < 0$), a positive difference between the vertical velocity in Aeolus and NoAeolus, (ω_A-ω_{nA}) > 0 means that Aeolus makes the upward motions weaker on average. With ($\omega_{nA} > 0$), negative differences between the vertical velocity in Aeolus and NoAeolus, (ω_A-ω_{nA}) < 0 mean that Aeolus makes the averaged downward motions weaker.

Table 3.1: Interpretation of the vertical velocity and its differences between the Aeolus and NoAeolus experiments.

	NoAeolus, ω_{nA}	Aeolus-NoAeolus, ω_A-ω_{nA}
Updrafts	$\omega_{nA} < 0$	(ω_A-ω_{nA}) > 0, Aeolus weakens updrafts
	$\omega_{nA} < 0$	(ω_A-ω_{nA}) < 0, Aeolus enhances updrafts
Downdrafts	$\omega_{nA} > 0$	(ω_A-ω_{nA}) > 0, Aeolus enhances downdrafts
	$\omega_{nA} > 0$	(ω_A-ω_{nA}) < 0, Aeolus weakens downdrafts

The results are shown in Fig. 3.7 for the three divergent mode types, the Kelvin, EIG and WIG waves, and in Fig. 3.8 for the Rossby and MRG waves. First of all, Fig. 3.7 makes it clear that the assimilation of Aeolus reduces the amplitudes of omega for all divergent modes. The result is consistent across all vertical levels and for the whole spectrum of ω. A negligible effect of Aeolus on the Rossby and MRG modes in Fig. 3.8 is coupled to very weak vertical velocities in quasi-rotational modes in the tropics, as seen in Fig. 3.3. Note that values in Fig. 3.8 are three orders of magnitude lower than for divergent modes.

The strongest Aeolus impact on omega on divergent modes is found in the troposphere. The effect maximizes around the 400-200 hPa levels, where convective updrafts are strongest. Note that in general the magnitude of changes in IG modes is 3-4 times stronger than for KW. Higher up in stratospheric levels, the Aeolus impact diminishes. An elongated tail at negative values between 200 hPa and 500 hPa for the EIG and WIG modes suggests that strong convective updrafts are concentrated in a relatively small number of grid cells. We do not see a similar effect for positive values of omega, possibly due to downwelling circulation being distributed over larger scales.

The result in Fig. 3.7 are consistent with the WP1 and TN1. We showed that Aeolus systematically reduces the amplitude of the horizontal winds associated with IG modes. The magnitude was estimated to be 10% and 7% for the WIG and EIG modes, respectively. On average, this implies a reduction in the amplitude of divergence, which in turn implies a reduction in the amplitude of vertical motions. A similar relative reduction is thus found in ω amplitudes in Fig. 3.7. The importance of the systematic effects should be evaluated together with Fig.3.3−Fig.3.6 that showed that effects are on average energetically negligible and noisy at small scales, where their amplitudes are largest. The systematic effects on the vertical velocity are not automatically expected to have an impact on averaged covariances terms, i.e. the VMFs.

The analysis of average Aeolus assimilation changes in ω from Figs. 3.7 and 3.8 was also performed for root-mean squared differences (RMSD), which are shown in Figures 3.9 and 3.10. The RMSD distributions much resemble the absolute values of systematic differences, meaning RMSD is largely dominated by them. Again divergent modes have values three orders of magnitude higher than those of rotational modes, again suggesting that Aeolus changes to vertical velocity for rotational modes is negligible.

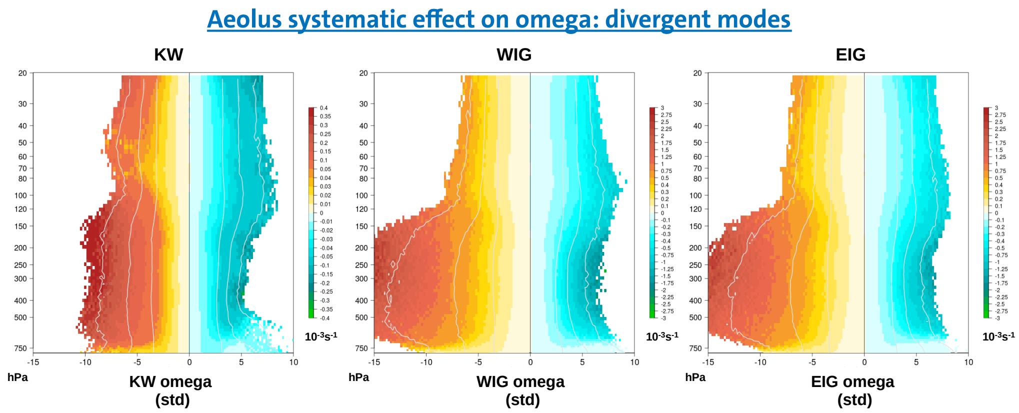

Figure 3.7: Systematic effects of the Aeolus wind assimilation of vertical pressure velocity ω associated with divergent modes: (left) Kelvin, (middle) EIG and (right) WIG modes. Color shading denotes average omega difference between Aeolus and NoAeolus experiments relative to NoAeolus omega for each wave type. All grid points from 10°S to 10°N in period July 2019−June 2021 period are used. Only values above the 99% significance level are plotted. Thin grey lines show sample sizes of 10^2, 10^3 and 10^4.

3.2.1 A note on $k = 2$ WIG ω

While analysing ω fields, we discovered a stationary large-scale structure of WIG omega in the stratosphere. It has $k = 2$ with stationary phase and amplitude and is found in both Aeolus and NoAeolus experiments throughout the study period. Examples on four random dates are shown in the Fig. 3.11.

It seems likely that the stationary $k = 2$ ω_W is an artefact of the assimilation system i.e. of the GOS. Indeed, a discussion with the ECMWF colleagues brought up a possibility that we diagnosed an orbital bias in the AMSU-A and ATMS observations, recently addressed by Bormann et al. (2023). Not that our diagnostic is very sensitive to such anomalies in the system and they will always appear in the IG modes. For example, Žagar et al. (2011) found that the covariance inflation derived from the sondes in the ensemble Kalman filter data assimilation at NCAR also caused a $k = 2$ WIG signal in the background covariances. The $k = 2$ was a signature of the global network of sonde observations, with sondes located primarily over the NH land areas. The artefact does not affect the diagnostic of the momentum fluxes, as shown in the next section.

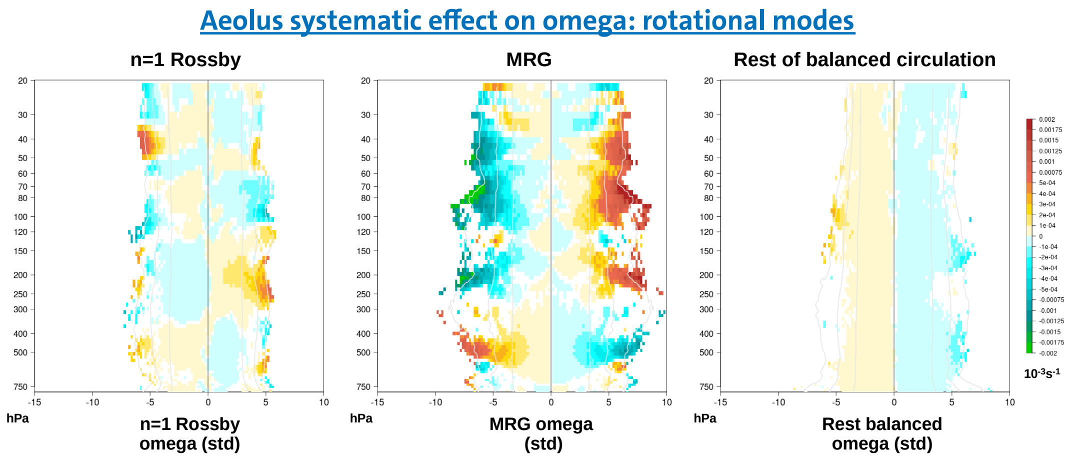

Figure 3.8: As in Fig. 3.7, but for rotational modes: (left) $n = 1$ Rossby, (middle) MRG and (right) $n > 1$ Rossby modes.

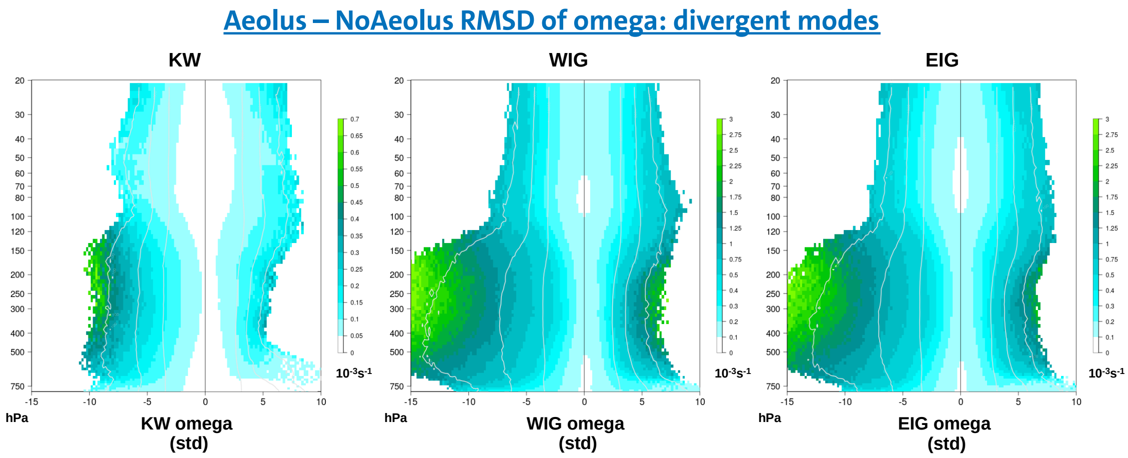

Figure 3.9: Root mean squared differences of Aeolus−NoAeolus vertical pressure velocity ω associated with divergent modes: (left) Kelvin, (middle) EIG and (right) WIG modes. Color shading: RMSD. All grid points from 10°S to 10°N in period July 2019−June 2021 period are used. Thin grey lines show sample sizes of 10^2, 10^3 and 10^4.

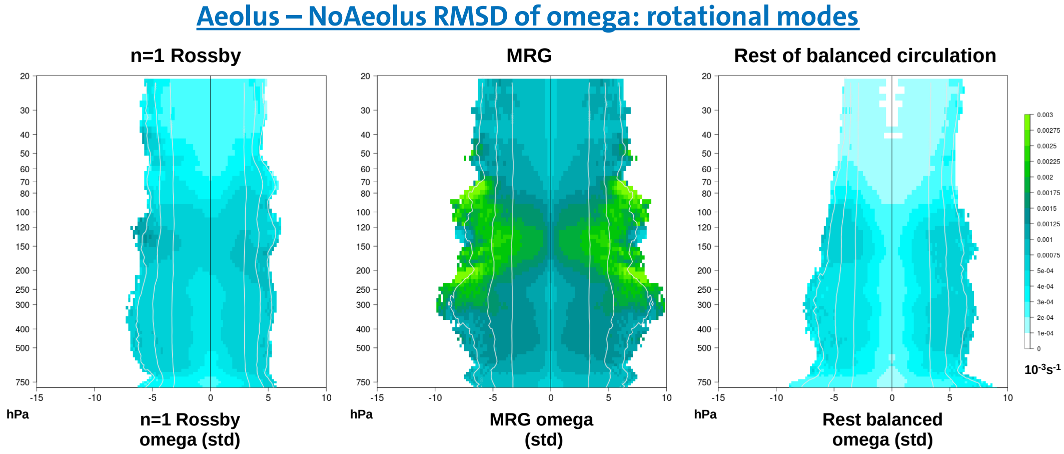

Figure 3.10: As in Fig. 3.9, but for rotational modes: (left) $n = 1$ Rossby, (middle) MRG and (right) $n > 1$ Rossby modes.

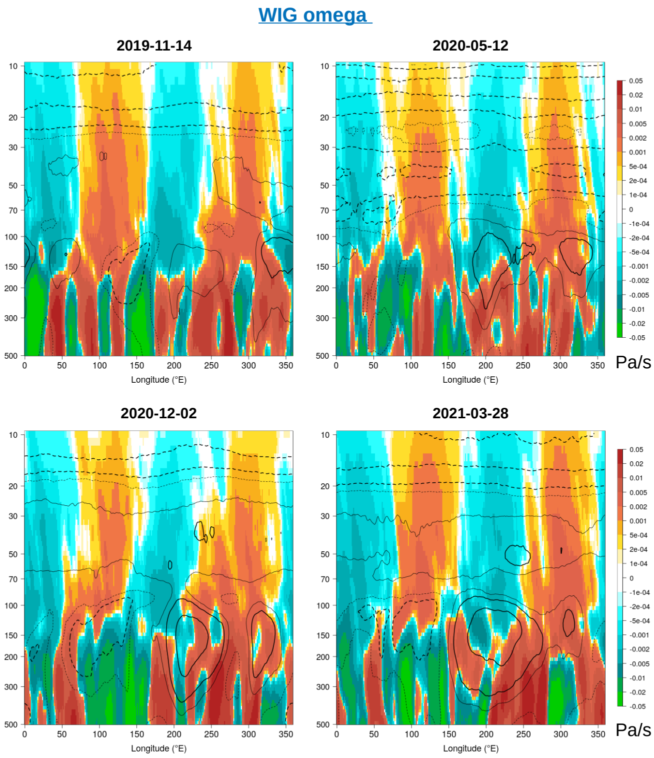

Figure 3.11: Vertical velocity omega associated with the WIG modes, ω_W, on four randomly selected dates from the NoAeolus experiment. Fields of ω_W smoothed by show 7-day running mean and averaged between 10°S$-$10°N and within ±5° longitude.

Chapter 4

Effects of Aeolus winds on the vertical momentum fluxes in the tropics

Now we analyze effects of Aeolus assimilation on the VMFs. In this chapter, we first present results in physical space before focusing on the scale distribution of differences. But first we provide an interpretation guide for this complex topic with the reference to the results of the WP1, and the QBO evolution. This guide also demonstrates that results of our calculations are in agreement with theory and previous studies of VMFs.

All results for the VMFs refer to the vertical flux of the zonal momentum i.e. the meridional momentum is not included unless specified. This is because the HLOS winds are nearly zonal. The effects on the meridional fluxes will be discussed in WP4 together with the comparison with the COSMIC2 data. Out of the 25 flux components listed in Table 1, we discuss 5 components which includes zonal wind perturbation for different modes and total vertical velocity, i.e. $\overline{\omega' u'_K}$, $\overline{\omega' u'_E}$, $\overline{\omega' u'_W}$, $\overline{\omega' u'_M}$ and $\overline{\omega' u'_R}$ as well as the total flux $\overline{\omega' u'}$. However, due to small amplitudes of the MRG zonal wind in deep tropics, the $\overline{\omega' u'_M}$ shows very small or negligible effects of Aeolus and is therefore not systematically presented.

4.1 Interpretation of the vertical momentum fluxes in relation to the flow

Although the calculation of VMFs is technically simple once the wave decomposition has been carried out, their interpretation is non-trivial. This section is meant to facilitate the interpretation of the results in the remainder of the chapter with respect to the background flow, the wave propagation (both horizontal and vertical) and the QBO state.

Figure 4.1 from TN1 shows the zonal-mean zonal wind evolution in the studied OSE period, including the QBO between 10-100 hPa and the zonal wind changes due to Aeolus superimposed in colours (in m/s). The areas highlighted with green circles are two specific periods of interest: the 2019/20 QBO disruption (left), and the classic downward QBO phase propagation (right).

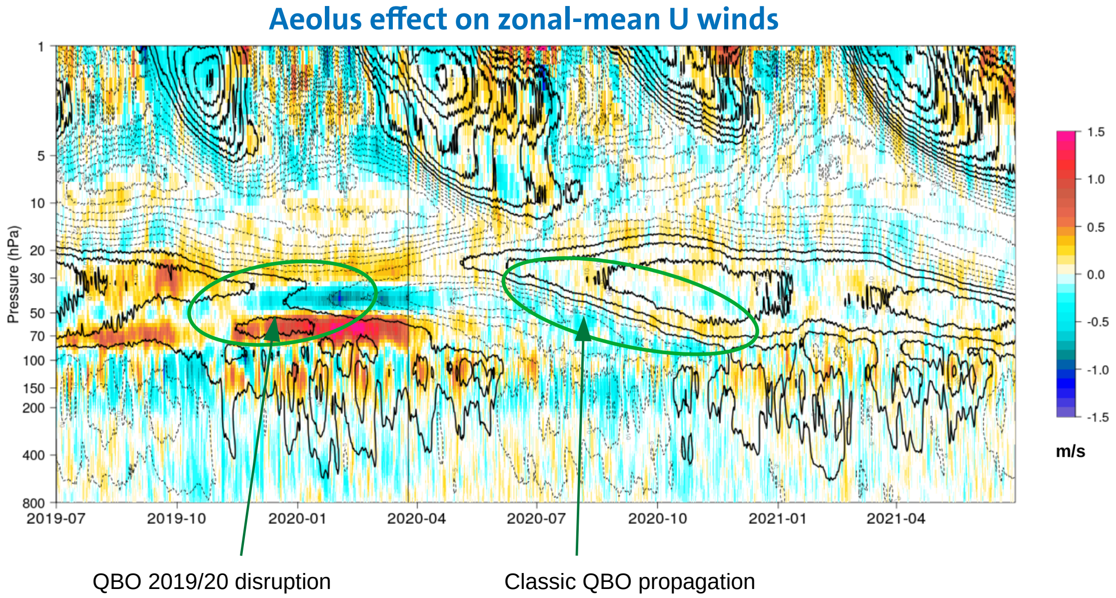

Figure 4.1: Aeolus effects on the equatorial zonal-mean zonal winds. Color shading: zonally averaged Aeolus-NoAeolus difference for the geostrophically balanced zonal wind (Rossby modes). Contour lines are zonal-mean NoAeolus winds: zero-wind line is first solid black line, with westerlies shown with solid black lines, and easterlies by thin dashed lines, with isoline spacing 5 m/s. Fields are averaged within 5°S and 5°N. Thin black vertical line on 2020-03-25 indicates the start of COSCMIC2 assimilation.

The strongest effect of Aeolus wind assimilation on the mean zonal winds is found during the 2019/20 QBO disruption, maximizing in period from December 2019 till February 2020. The largest changes are aligned with the appearance and strengthening of the newly formed easterly core at 40 hPa and the remaining westerly core below at 70 hPa. The overall positive effect of Aeolus is an increase in the vertical wind shear. Following the start of the COSMIC2 assimilation, the magnitude of Aeolus−NoAeolus differences decreases, but it can be still clearly seen that Aeolus increases the vertical gradient of the zonal wind during the classical downward propagation of the westerly QBO phase from August 2020 till November 2020. This is seen as positive changes in the zonal-mean zonal wind within westerlies (i.e. strengthening of the westerlies), and negative changes within easterlies (i.e. strengthening of the easterlies).

There are several possible sources of the Aeolus−NoAeolus differences in the mean zonal winds. First of all, the QBO disruption was an extreme event which was not forecast. Given the absence of the signal in the first-guess field for the assimilation and the observation memory of the system, it took time for the system to react to new observations, as noted for ERA5 by Banyard et al. (2024). As the event likely remained poorly represented in short-term forecasts and other observations were less informative about dynamical processes, Aeolus observations remained valuable throughout the disruption. Their effect was likely twofold: first, Aeolus data helps to correct the wind field in the lower stratosphere by observing it *in situ*, and second, by changing the representation of the vertically-propagating equatorial waves and how they interact with the mean flow, which is the mechanism by which the QBO phase changes are forced. Another possible indirect effect is the offset of the effects of vertical diffusion on the vertical shear of the zonal wind by the Aeolus assimilation. Since VMFs describe the momentum transport and deposition by atmospheric waves, their analysis will provide a better understanding on what processes have been affected by Aeolus.

A guide on the relation of the QBO phases, equatorial waves and their properties regarding propagation and momentum transport is presented in Fig. 4.2. The top panel shows the alternating westerly (grey shading) and easterly (white) QBO phases. The diagrams on the bottom left from Wheeler and Kiladis (1999) show various equatorial wave types in the wavenumber-frequency domain in the symmetric and asymmetric parts of the spectrum. The x-axis is the zonal wavenumber, and the y-axis is the wave frequency. The eastward-propagating waves are marked with green arrows and green circles; these are the KW and EIG waves that appear in the $k > 0$ part of the wavenumber-frequency diagrams. In terms of *vertical* propagation, KW and EIG waves can propagate upward within easterly background winds according to linear theory. This defines their location in the top panel with QBO evolution with the green arrows.

As a rule-of-thumb, the zonal momentum transported vertically by eastward-propagating equatorial waves, i.e. by the KW and EIG waves, has an opposite sign to the background flow within which the wave propagate (e.g. Andrews et al., 1987). This means that the KW and EIG waves are transporting westerly momentum upwards (green arrows) within easterly background winds. Eventually they encounter their critical level (i.e. a level where the wave speed is equal to the background flow speed), and wave breaking and momentum deposition take place. The westward momentum deposited near the critical level by the KW and EIG waves exerts a westerly drag on the mean easterly flow. This effectively lowers the zero wind line, and slowly forces the downward progression of the westerly QBO phase. With the VMFs presented in pressure units as $-F/g$, the upward transport of westerly momentum is positive, as highlighted in the green box in the bottom right part of Fig. 4.2.

The westward-propagating waves are marked red in Fig. 4.2; the Rossby, MRG and WIG waves belong to this group. These waves propagate upward most easily within westerly winds, as marked with the red arrows in the top panel. They transport easterly momentum, and deposit it around the zero-wind line thereby exerting easterly drag on the mean westerly flow. This leads to the downward progression of the easterly QBO phase above the zero wind line. The upward transport of easterly momentum is negative, as highlighted in the red box in the bottom right part of Fig. 4.2.

A summary of the interpretation of VMFs is as follows:

1. The upward transport of westerly momentum by the eastward-propagating KW and EIG waves can be recognized by positive values of the VMF ($-F/g > 0$), and

2. The upward transport of easterly momentum by westward-propagating Rossby, MRG and WIG waves will appear as a negative vertical flux of the zonal momentum, ($-F/g < 0$).

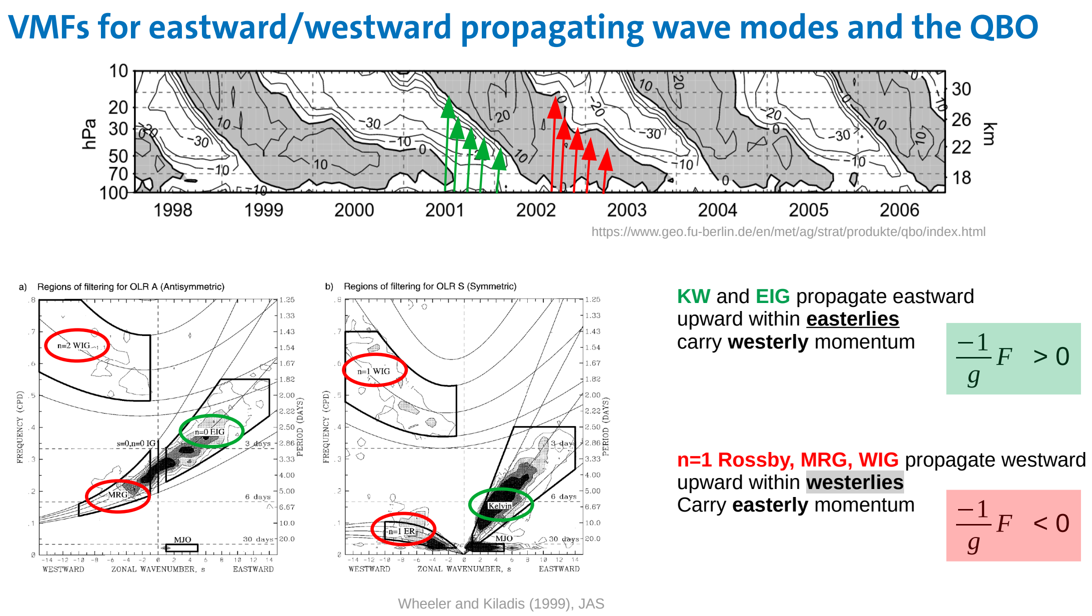

Figure 4.2: Interpretation of the vertical momentum fluxes in the context of wave propagation and the QBO.

4.1.1 Examples of VMFs from the OSE

We now test whether computed VMFs agree with theoretical expectations for a given wave type and the background flow. Figure 4.3 shows longitude-pressure examples of VMFs from the NoAeolus experiments on two dates in April 2020, after the application of the 7-day running mean. The vertical fluxes of the zonal momentum are shown separately for the KW, EIG and WIG waves overlaid on the background winds. In April 2020, the stratosphere between 70 hPa and 10 hPa was dominated by easterlies, an environment in which the Kelvin waves propagate vertically. In the upper troposphere (100-200 hPa), there were regions with easterlies and westerlies, with westerlies found in 180-250°E and near 320°E.

Given the background flow, the KWs are able to propagate vertically in the stratosphere. Indeed, positive KW VMF is found throughout the stratosphere in Fig. 4.3 (left). In the upper troposphere, the KW VMF is a mix of positive and negative fluxes, with the strongest positive flux in the western hemisphere within background easterlies. Note also that the stratospheric layer directly above the upper-troposphere core of easterlies has relatively larger VMF (green arrows) than the rest of the stratosphere.

The EIG wave VMF on a different date shows a similar structure to the KW VMF (Fig. 4.3, middle). There is a positive VMF indicating upward zonal momentum transport by EIG waves within easterlies, with a strong longitudinal gradient near the dateline where upper-tropospheric easterlies are replaced by westerlies.

The right panel in Fig. 4.3 shows the WIG wave VMF on the same day as for the EIG wave VMF. As discussed above, the upward momentum transport by WIG is indicated

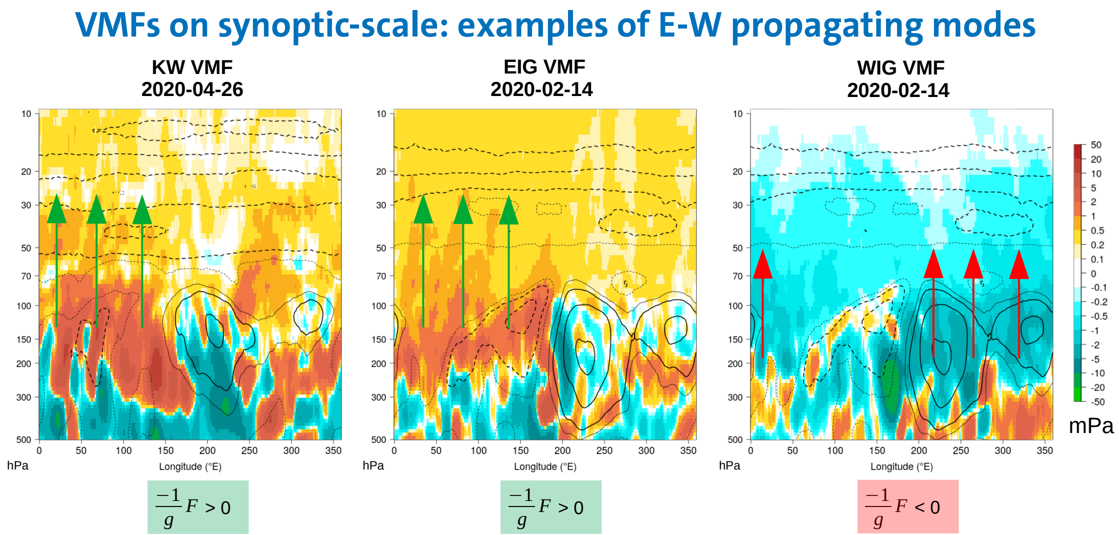

Figure 4.3: Examples of vertical fluxes of the zonal momentum for (left) Kelvin waves ($\overline{\omega' u'_K}$), (middle) EIG waves ($\overline{\omega' u'_E}$) and (right) WIG waves ($\overline{\omega' u'_W}$). Color shading: VMFs. Contours denote the zonal wind, with solid lines for westerlies and dashed lines for easterlies at 5 m/s interval, starting at ±2 m/s which are shown as thin contours. The direction of the vertical momentum transport is indicated by arrows. Averaging is for 10°S-10°N, ±5° longitude, and 7-day running mean.

by negative VMFs. The largest negative VMFs are found within the upper-tropospheric westerlies (red arrows) in the eastern Hemisphere. Due to stratospheric easterlies, WIG wave VMFs seem to dissipate completely by the time they reach 15 hPa. For comparison, EIG waves propagate at least up to 10 hPa.

The examples shown in Fig. 4.3 demonstrate the ability of our VMF method to filter wind anomalies belonging to each wave type from instantaneous 3D fields. Without using the time-dimension, EIG and WIG are properly separated, giving the right VMFs expected from linear theory even at synoptic scales, on the same day, within the regions where background winds support the vertical propagation. This reassures the robustness of the results presented later in this Chapter.

Because of a large intermittency of IG waves and their fluxes, the examples in Fig. 4.3 include 7-day running mean as well as the latitudinal (10°S-10°N) and longitudinal ±5° longitude) averaging. This ensures that the VMFs show coherent and smooth structures easy to interpret. However, the Aeolus−NoAeolus VMF differences are difficult to interpret the same way, as they appear very patchy (not shown). Therefore, the focus of physical-space analysis will be on zonally-averaged differences between the Aeolus and NoAeolus VMFs.

4.1.2 VMFs and wave-mean flow interactions

The zonal-mean VMFs can be used to diagnose equatorial wave interactions with the mean flow. The vertical gradient of the VMF, $\partial F/\partial p$ indicates vertical divergence of the momentum transport, its deposition and the drag it exerts on the zonal mean flow. This is demonstrated in Fig. 4.4 which shows the time-height evolution of the zonally-averaged KW VMFs (Fig. 4.4a), and the resulting drag exerted by the VMFs (Fig. 4.4b).

The KW VMFs are positive in the upper troposphere and stratosphere, and are found at higher levels within the easterly phase of the QBO, as marked by the green arrows from May 2020 till October 2020 in Fig. 4.4a. The VMFs decrease abruptly as soon as they cross the zero-wind line (first solid black contour line). As the KWs transport the westward momentum upward, its deposition near critical lines exerts a westerly drag on the mean flow, i.e. a positive zonal wind forcing. In Fig. 4.4b, the drag exerted by the KW VMF appears positive (yellow-red shading) most of time, and it maximizes just below the zero-wind line as the westerly QBO phase is progressing downward, as expected from the interaction of the KWs with the zonal-mean background flow.

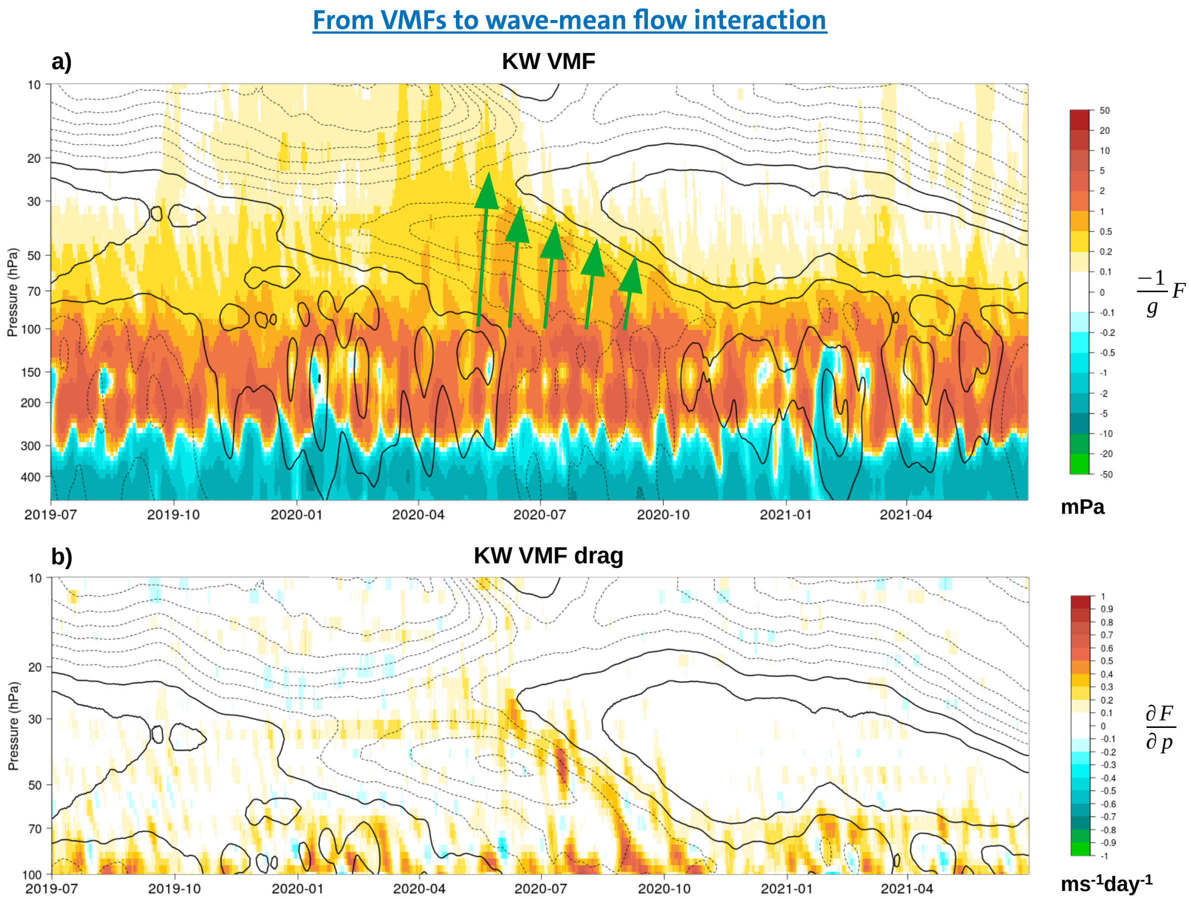

Figure 4.4: Illustration of wave−mean flow interactions for the Kelvin wave VMFs, $\overline{\omega' u'_K}$. (a) Time-height evolution of the Kelvin wave zonal-mean VMF in the NoAeolus experiment, with vertical momentum transport indicated by arrows. (b) Resulting wave drag from the VMF vertical gradient, $\partial F/\partial p$. Contour lines are zonal-mean zonal winds, with the same contouring as in Fig. 4.1. See text for details.

In summary, this section provided a guide for the interpretation of VMFs in relation to different wave types, their propagation and the QBO. Proof-of-concept of the applied methodology shows that MODES filtering and VMF calculations lead to results expected from linear theory. The outlined interpretation is applied in the next section focusing on the stratosphere between 100 hPa and 10 hPa and differences between Aeolus and NoAeolus OSEs.

Note that the tropospheric VMFs, especially below 200 hPa are not discussed, as the theoretical framework applies to adiabatic dynamics. Below 200 hPa, moist tropical processes increasingly interfere with the dynamical fluxes making interpretation difficult.

4.2 Fluxes in physical space

Now we present the VMFs for $\overline{\omega' u'}$ and its components associated with u' contributions of different wave species. Vertical fluxes of the meridional wind, $\overline{\omega' v'}$, which are not discussed, are much smaller and do not interact with the QBO zonal winds. The zonal-mean meridional wind in the tropics is zero.

Note that the vertical flux of the zonal wind is only one term of the full Eliasen-Palm (EP) flux vector; other terms include heat fluxes ($\overline{v'\theta'}$, where θ' is the potential temperature perturbation, and the horizontal momentum fluxes $\overline{u'v'}$. Heat fluxes are known to be dominated by vertical propagation of the $n = 1$ Rossby and MRG mode θ' (e.g. Kim and Chun, 2015a). The horizontal momentum fluxes include the impact of extratropical waves penetrating the tropics. A full EP-flux budget, similar to the one computed by Kang and Chun (2021), is possible with MODES, is however not a part of WP2. Therefore, the analysis of the 2019/20 QBO disruption will not discuss the extratropical Rossby wave forcing of the event propagating. We focus on the effects of Aeolus winds to sustain or enhance equatorial wave forcing of the developing easterly core at around 40 hPa and the remaining westerly core near 70-80 hPa.

The VMF analysis in physical space is divided into three subsections as follows: first we describe the Aeolus effect on the total VMF, then discuss the components due to the eastward- and westward-propagating waves. In all cases, the calculations use total ω' as discussed in Methodology section.

4.2.1 Aeolus effect on total VMFs

Evolution of VMFs and their drag

Figure 4.5a shows the evolution of the total VMF $\overline{\omega' u'}$ as function of pressure in the NoAeolus experiment ($-F/g$). Significant positive fluxes are present within the easterly wind regime (yellow-orange shading), indicating upward transport of westerly momentum by the eastward-propagating waves. Mostly negative fluxes of lower magnitudes are found within the westerly QBO phases. This indicates an overall smaller momentum transport by all wave types. Both westward and eastward propagating wave types are present specially in the lower stratosphere within westerly QBO phase: the weaker (compared to the easterly phase) westerlies allow for some eastward propagating waves to travel vertically as well, although this regime is more typical for westward propagating waves.

The drag exerted by the total VMF on the zonal-mean zonal wind is shown in Fig. 4.5c. Transitions from the westerly QBO (WQBO) to easterly QBO (EQBO) are seen in the following periods: July-November 2019 around 20 hPa, October 2020 till June 2021 progressing from 20 hPa down to 50 hPa, and February-May 2020 at 50-70 hPa. In WQBO to EQBO transitions, the blue color shading indicates an easterly zonal-mean zonal wind acceleration by the deposition of the VMF (vertical convergence). This is the dynamics expected from wave−mean flow interaction forcing of the QBO phases. A mirror image can be noticed in the EQBO to WQBO transition in July-October 2020 from 30 hPa down to 70 hPa; orange-red color shading indicates westerly acceleration of the zonal-mean zonal wind by the deposition of the total VMF. The E-W zonal-mean zonal wind changes around 10 hPa (and above, not shown) are associated with the stratospheric semi-annual oscillation, not discussed in this TN.

In Fig. 4.5c, the VMF drag that forces the QBO transitions has a smaller amplitude during W to E transitions (blue-green shading within easterly shear lines), than that of E to W QBO transitions (orange-red shading within westerly shear lines). This agrees with different magnitudes of QBO phase change forcing reported by Kim and Chun (2015b). The sign, amplitude and dynamics of VMF drag in Fig. 4.5c are comparable to previous studies (Kim and Chun, 2015a,b; Kang and Chun, 2021).

Aeolus−NoAeolus VMF differences

We proceed with Aeolus−NoAeolus differences in total VMF and its drag, which are shown in Fig. 4.5b and Fig. 4.5d, respectively. For their interpretation, it is important to keep in mind the evolution of zonal-mean zonal wind differences (Fig. 4.1 in Section 4.1). As discussed earlier, the assimilation of Aeolus winds increased vertical shear of the QBO winds both during the 2019/20 QBO disruption, especially from December 2019 till February 2020, and during the classical downward propagation of the westerly QBO phase from August 2020 till November 2020.

During the 2019/20 QBO disruption, Aeolus−NoAeolus differences in VMF (Fig. 4.5b) resemble the changes in the zonal-mean zonal winds (Fig. 4.1). From December 2019 till April 2020, Aeolus acts to strengthen the newly formed easterly core at 40 hPa which is seen as negative zonal wind differences and negative differences in VMF (blue-green shading). Simultaneously, Aeolus strengthens also the remaining westerly core near 70 hPa which is recognized as positive VMF differences in Fig. 4.5 (orange-red shading).

When equatorial waves propagating vertically from the upper troposphere encounter slightly strengthened westerlies at 70 hPa, the westward-propagating waves carrying the easterly momentum (VMF$<$0) are able to propagate higher up i.e. to to carry the momentum slightly higher above the westerly core. On the other hand, the eastward propagating waves carrying the westerly momentum (VMF$>$0) encounter an environment that inhibits vertical propagation. Thus, the positive VMF remains within the westerly core. Both processes can lead to the VMF differences presented in Fig. 4.5b during the disrupted 2019/20 QBO. A detailed analysis for different wave species is needed to determine for which wave type Aeolus has the largest effect on VMFs. For the total fluxes during the 2019/2020 disruption, the most plausible explanation is that VMFs are interacting with changes in zonal-mean zonal winds.

The associated changes in drag, corresponding to differences in the vertical gradients of the total VMF, are shown in Fig. 4.5d. Changes in the drag are not aligned with the changes in zonal-mean zonal winds; negative drag differences are largest in the upper half of the easterly core whereas the largest positive drag differences can be seen in the bottom half of the easterly core.

Note that Aeolus−NoAeolus total VMF and drag differences in Fig. 4.5 sharply decrease in magnitude after the start of COSMIC2 assimilation (vertical line on 2020-03-25). The assimilation of COSMIC2 measurements within the ECMWF system strongly improved wind forecasts in the tropical upper-troposphere and stratosphere (Ruston and Healy, 2021a). We also showed earlier in Fig. 4.1 and in TN1 that Aeolus effects on equatorial waves and zonal-mean flow became smaller after the start of the COSCMIC2 assimilation in the OSE. We relate these results to the much higher observation density delivered by COSMIC2 compared to earlier GNSS-RO missions (Schreiner et al., 2020), which is able to constrain a part of the tropical wind field observed by Aeolus.

The effect of Aeolus during the classical downward propagation of the westerly QBO phase is also to increase the vertical wind gradients although with a smaller magnitude. The Aeolus−NoAeolus VMF difference during July-October 2020 has a patchy appearance (Fig. 4.5b). However, a more consistent structure emerges when the vertical gradient of VMF differences is considered (Fig. 4.5d). For weak easterlies ($-5 < u < 0$ m/s), the Aeolus−NoAeolus VMF drag difference is intermittent but consistently negative throughout July-October 2020 (blue shading between the first solid line and first dashed line). For weak westerlies ($0 < u < 5$ m/s), the VMF drag difference is patchier, but the positive sign prevails.

Martin et al. (2023) reported largest forecast improvements from Aeolus assimilation in the global ICON model around the above discussed transition from QBO easterlies to westerlies. This was linked to the QBO range bin setting available once per week in the Aeolus measurements, which provided wind observations higher up to 25 km. Our results here suggest that in the ECMWF system, wave-mean flow interactions (the above discussed drag changes) are also affected throughout the QBO phase downward progression.

In summary, Aeolus effects on the VMF drag during this classical QBO phase transition are in alignment with changes in the the zonal-mean zonal wind and not the VMFs. This suggests that the VMFs changes are not due to differences in the zonal-mean zonal wind, but rather due to changes in the wave-mean flow interactions that drive the QBO phase transitions and are influenced by the assimilation of Aeolus winds. In other words, Aeolus winds affect wave-mean flow interactions. Understanding this effect was helped by analysing both the VMFs and associated drag and how they align with the effects in the zonal wind.

Now we carry out the same analysis for different wave types.

4.2.2 Effects on fluxes due to the eastward-propagating waves

Figure 4.6 shows the VMF and drag associated with the Kelvin waves and their Aeolus−NoAeolus differences. The VMF and drag resemble those of the total VMFs, especially during the 2019/20 QBO disruption. A positive KW VMF drag around 30 hPa, that bridges the dissipating westerly QBO upper core by the end of 2019 and the onset of a new westerly QBO phase in June 2020 near 25hPa, can be seen in Fig. 4.6c. A similar but stronger KW forcing during the 2015/16 QBO disruption is known to have sustained the upper westerly QBO core, which in that case did not dissipate (Kang et al., 2020). A significantly weaker KW activity during the 2019/20 disruption could not sustain the upper part of the westerly QBO core around 30 hPa (Kang and Chun, 2021). The effect of Aeolus winds was to reduces the KW forcing between the westerly QBO phases (Fig. 4.6c-d).

Kelvin waves dominates the forcing of the EQBO to WQBO transition with their westerly momentum deposition near the zero wind line, as can be observed in July-October 2020 in Fig. 4.6c as the positive drag ($\partial F/\partial p > 0$, red shading). However, this is barely affected by Aeolus assimilation as no discernible differences can be seen in Fig. 4.6d during that time.

Figure 4.7 shows the VMF and drag analysis for the EIG modes. In the lower stratosphere, the EIG wave VMFs have similar magnitude to those of KWs. Within 30-50 hPa layer and above, the EIG drag becomes clearly dominant over that of KW. This implies that less EIG VMF compared to KWs is being deposited to affect the zonal-mean zonal flow (light yellow shading in Fig. 4.7c), which is apparent during the classical E-W QBO transition in July-October 2020.

The Aeolus−NoAeolus EIG VMF differences are prevalent negative (Fig. 4.7b) indicating that Aeolus reduces EIG VMF, especially during the 2019/20 QBO disruption. Changes in the wave drag are however very small (Fig. 4.7d).

4.2.3 Effects on fluxes due to the westward-propagating waves

Figure 4.8 shows the VMF and drag analysis for the $n = 1$ Rossby wave, the most energetic among the Rossby modes. It was shown in TN1 to be affected by Aeolus in a similar way like the Kelvin wave. Negative $n = 1$ Rossby wave VMF exist within westerlies or weak easterlies (Fig. 4.8a), as expected. The exerted easterly drag in Fig. 4.8c occurs near the lines of the WQBO to EQBO transitions, as expected. However, the magnitude of $n = 1$ Rossby drag is very small compared to that of the Kelvin waves, which is also an expected feature of the drag due to the vertical flux of the horizontal $n = 1$ Rossby wave momentum. The Aeolus−NoAeolus differences in VMF and drag attributed to the $n = 1$ Rossby waves (Fig. 4.8b and Fig. 4.8d) generally follow the corresponding patterns for total VMF (Fig. 4.5). During the 2019/20 QBO disruption there is a strong similarity to the KW response (Fig. 4.6).

Finally, Fig. 4.9 shows the VMF and drag analysis for the WIG modes. The upward-propagating WIG waves are characterized by negative VMFs, adding the easterly momentum transport to the mean zonal wind. The WIG wave VMF amplitudes in Fig. 4.9a have maxima within westerlies and the exerted easterly drag follows W-E QBO transitions in Fig. 4.9c. The magnitudes of WIG wave VMFs and drag surpass those of the $n = 1$ Rossby wave.

During the 2019/20 QBO disruption, Aeolus−NoAeolus differences in WIG wave VMF and drag (Fig. 4.9b and Fig. 4.9d, respectively) have opposite signs of those for the Kelvin waves and $n = 1$ Rossby waves. Previously we hypothesized that total, Kelvin and $n = 1$ Rossby wave VMF differences happened in response to changes in zonal-mean zonal wind, i.e. strengthening of the easterly core at 40 hPa and westerly core at 70 hPa. In the case of WIG, it is plausible that a somewhat earlier onset of a slightly stronger easterly core in the Aeolus experiment enabled the downward progression of the shear lines to start earlier. This is suggested by the collocation of easterly WIG drag at 50 hPa at the end of 2019−beginning of 2020 (blue shading in Fig. 4.9c), and the negative Aeolus−NoAeolus differences in the WIG drag (blue shading in Fig. 4.9d).

4.2.4 Summary of the VMF analysis in physical space

The interpretation of Aeolus effects on the VMF demonstrates the usefulness of evaluating the wave fluxes and drag simultaneously in the context of wave−mean flow interactions during the QBO phase changes and the 2019/20 QBO disruption. This approach unveiled the effects of Aeolus on equatorial waves, which go beyond maintaining/increasing the vertical shear of the horizontal wind reported in TN1.

Aeolus assimilation affects interactions of equatorial waves with mean flow via two different mechanisms. First, the VMFs associated with the Kelvin and $n = 1$ Rossby wave zonal winds change in accord with the changes in the zonal-mean zonal winds due to Aeolus winds. This was the case during the 2019/20 QBO disruption in the lower stratosphere. In the second mechanism, Aeolus winds directly contribute to the transition from the easterly to westerly QBO phase. During the classical downward propagation of the westerly QBO phase in summer and autumn 2020, the EIG wave drag differences due to Aeolus were aligned with the zonal-mean zonal wind changes, but not with the EIG wave VMFs. A similar effect could be observed during the WQBO to EQBO transition at the beginning of 2020, when Aeolus affected the WIG wave VMFs and drag.

We also note that the same analysis was performed for the MRG waves, but it is not shown due to much smaller effects of Aeolus for reasons discussed above.

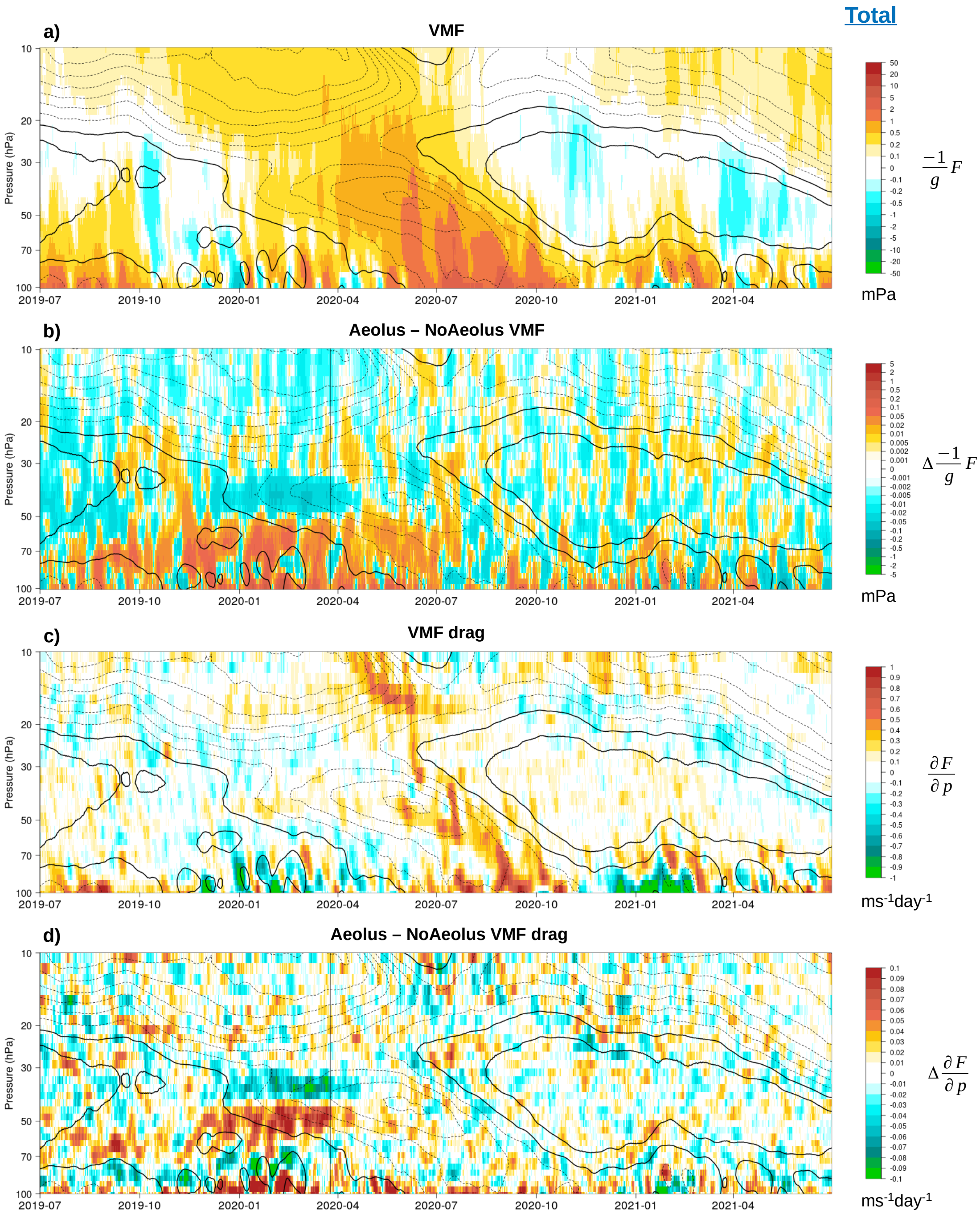

Figure 4.5: Aeolus effects on the total VMF and wave−mean flow interaction. (a) evolution of the zonal-mean VMF in NoAeolus experiment. (b) As a) but for Aeolus−NoAeolus. (c) As a) but for wave drag. (d) As c) but for Aeolus−NoAeolus wave drag. Thin black vertical line in b) and d) indicates the start of COSCMIC2 assimilation on 2020-03-25. Contour lines are zonal-mean zonal winds, starting from the zero wind line. Full black and thin dashed lines correspond to westerlies and easterlies, respectively, every ±5 m/s.

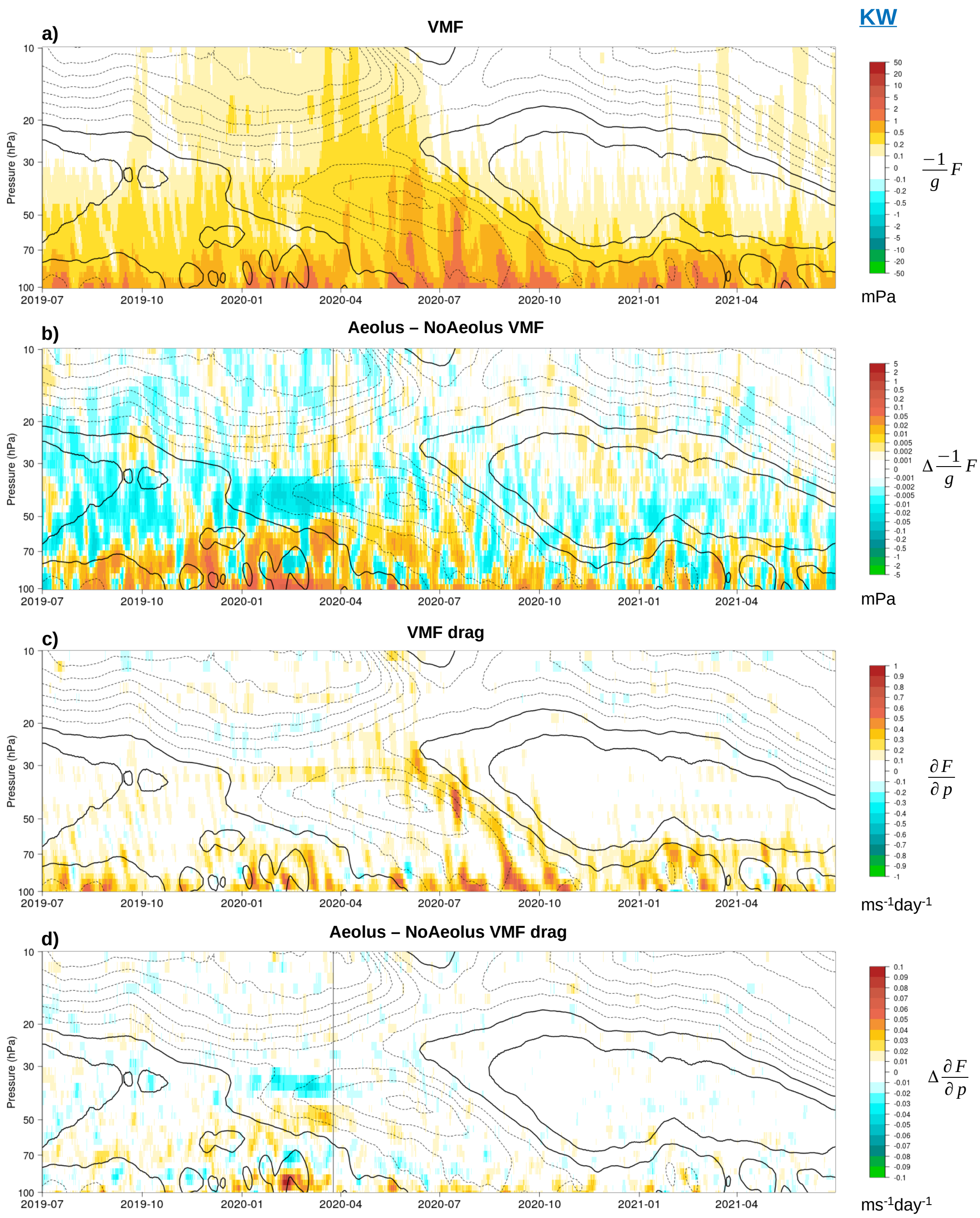

Figure 4.6: As in Fig. 4.5, but the Kelvin waves, $\overline{\omega' u'_K}$.

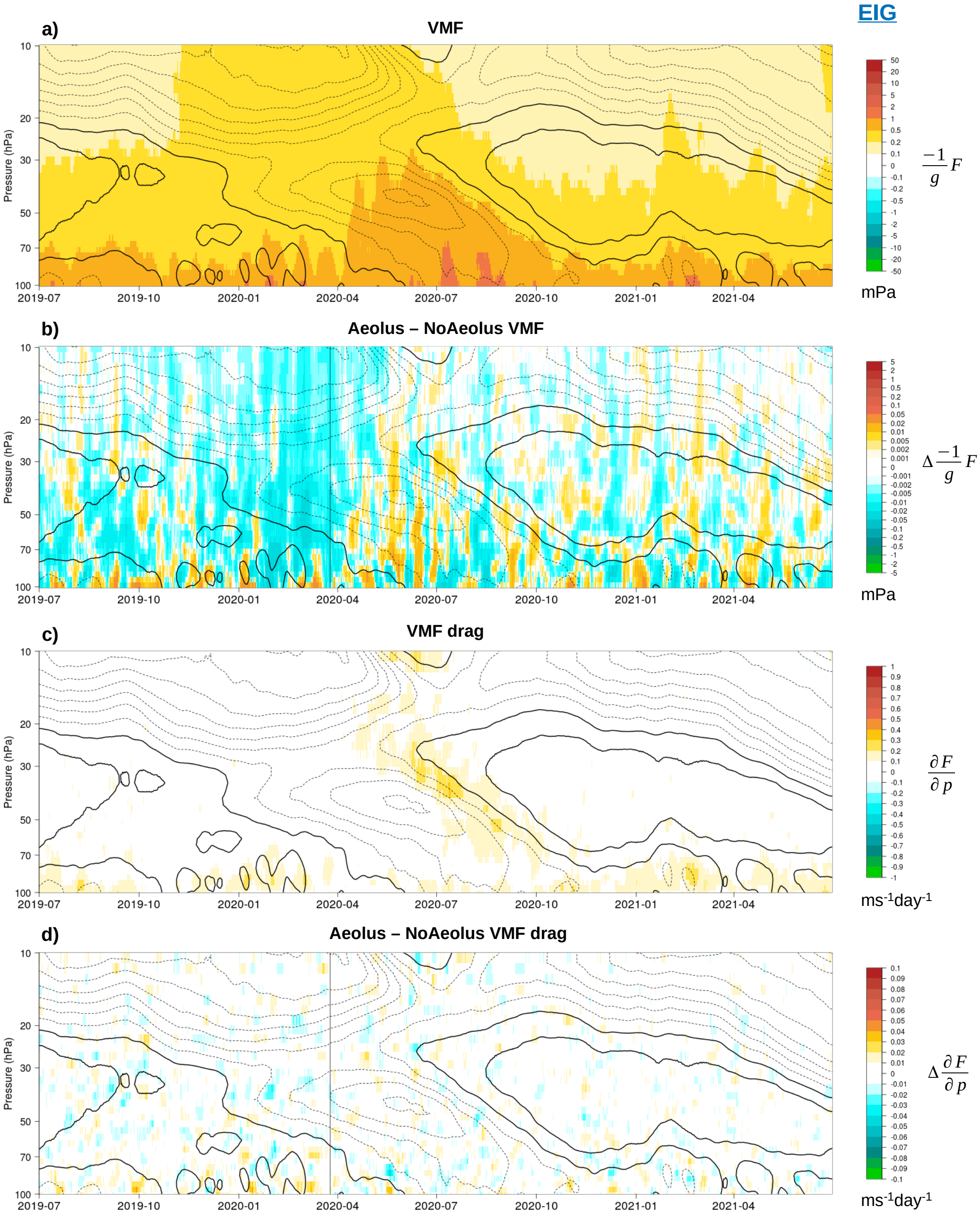

Figure 4.7: As in Fig. 4.5, but for the eastward-propagating inertia-gravity modes, $\overline{\omega' u'_E}$.

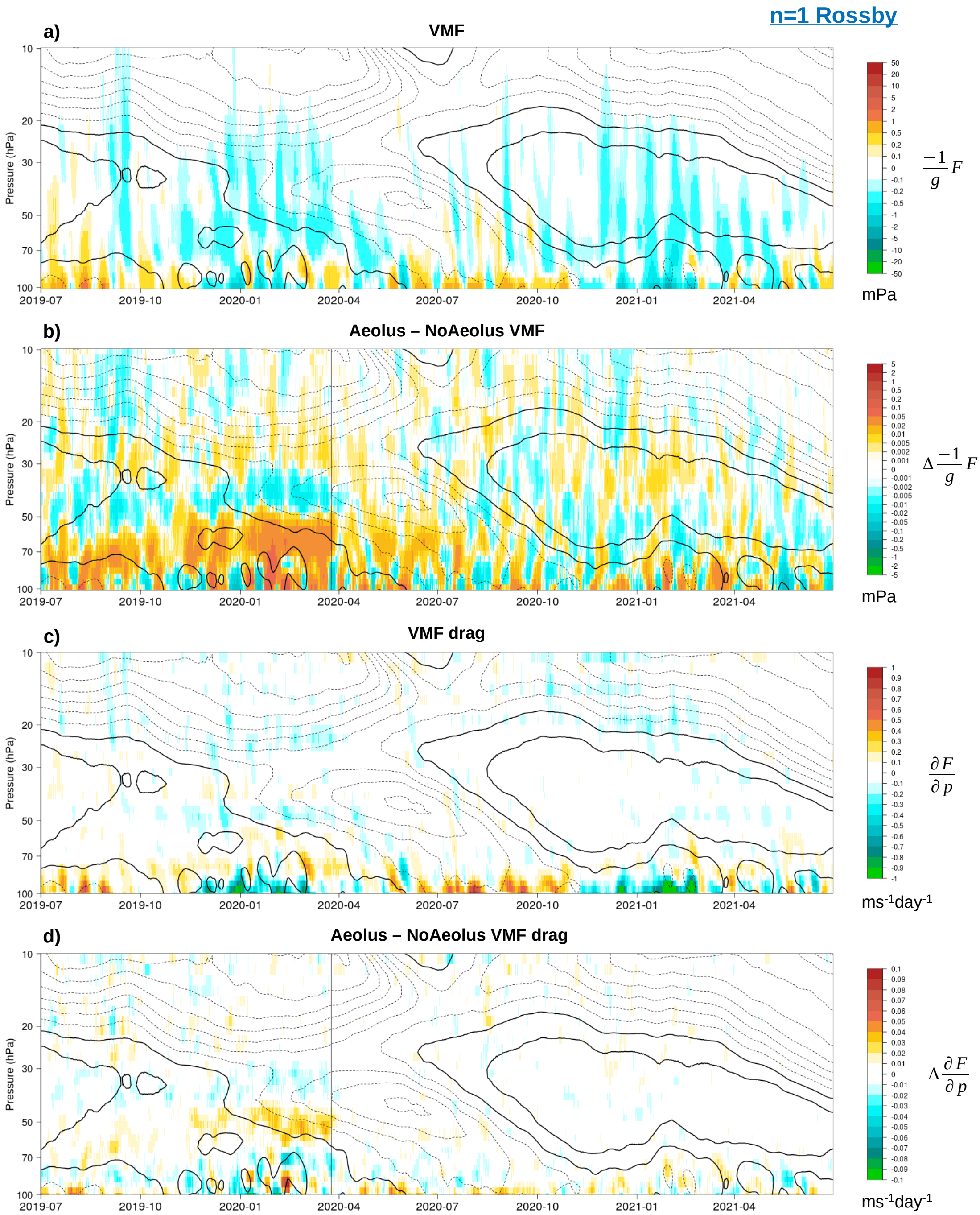

Figure 4.8: As in Fig. 4.5, but the $n = 1$ Rossby wave, $\overline{\omega' u'_{n1R}}$.

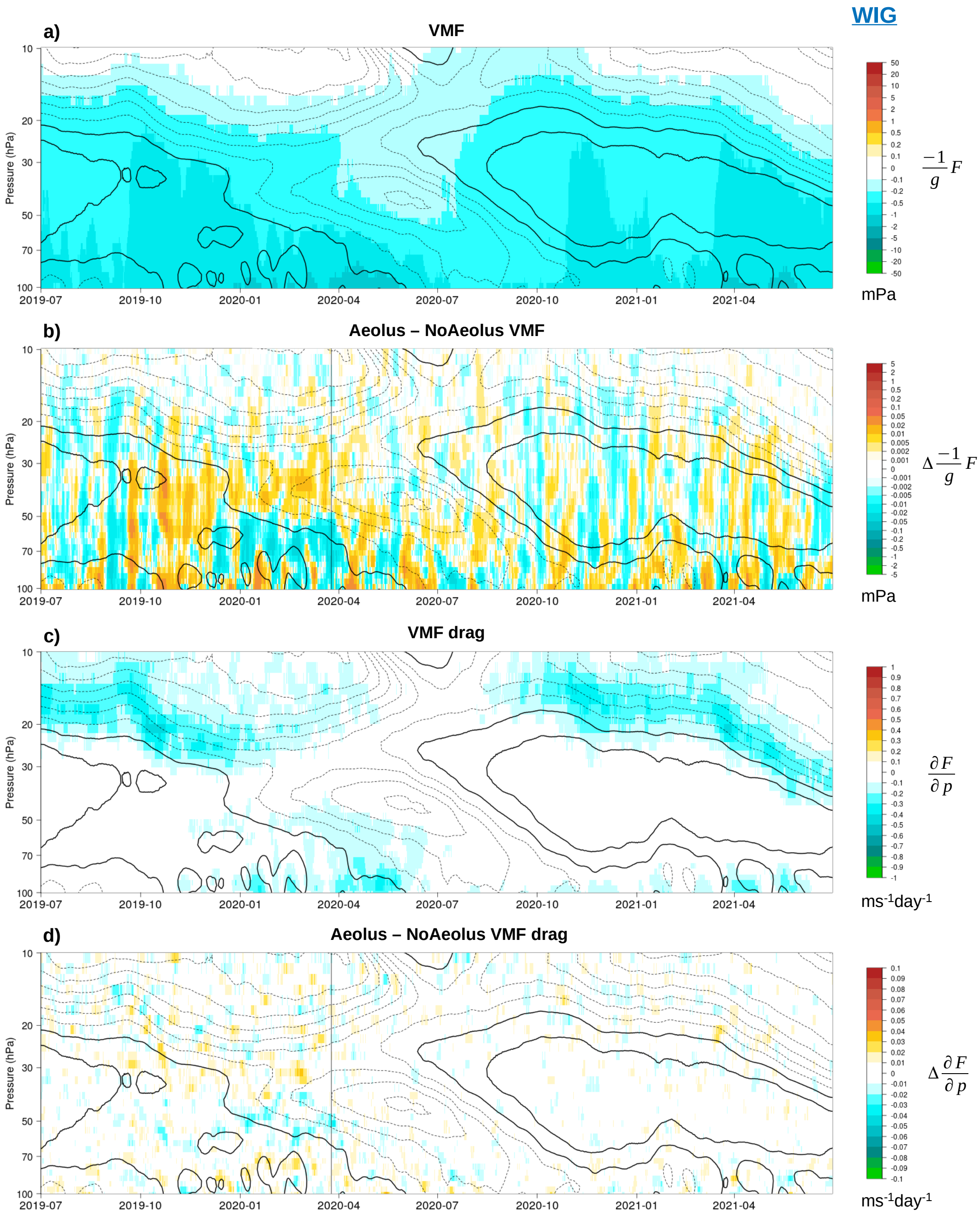

Figure 4.9: As in Fig. 4.5, but the westward-propagating inertia-gravity modes, $\overline{\omega' u'_W}$.

4.3 Cospectra of the momentum fluxes in relation to the flow

Now we present scale-dependent VMFs associated with different wave species. The key question is the following: what scales of the VMFs are most affected by Aeolus winds and how significant is the change with respect to the experiment which did not assimilate Aeolus? The results discussed so far revealed that Aeolus effects decreased significantly after spring 2020, in line with increasing observation error and the introduction of the COSMIC2 data in the assimilation. The latter will be quantified relative to Aeolus in WP4. While it is impossible to accurately quantify flow dependency of Aeolus effects, discussion in the previous sections demonstrates that our methodology provides coupling of the equatorial wave dynamics and VMFs with the background flow.

For a compact presentation, we choose to present several representative months including the period of the QBO disruption, and more normal evolution of the QBO during boreal summer 2020. Out of 25 components of the zonal momentum flux listed in Table 1, we discuss $\overline{\omega' u'_K}$, $\overline{\omega' u'_E}$, $\overline{\omega' u'_W}$, $\overline{\omega' u'_M}$ and $\overline{\omega' u'_R}$ cospectra as well as the total flux $\overline{\omega' u'}$.

The averaging is performed similar to that for the vertical velocity, over latitude belt 10°N-10°S. Monthly averaging follows 7-day running mean applied to every zonal wavenumber k. All model levels above 100 hPa are analysed up to the zonal wavenumbers $k = 150$.

The wavenumber spectra of the horizontal wind are red, while the VKE spectra discussed in Section 3.1 are more shallow and ideally nearly white for the IG waves. The momentum flux spectra therefore should also follow power laws in the resolved range of scales by the ECMWF model. Previous modelling studies suggest that the power laws for the momentum flux zonal wavenumber spectra in the middle atmosphere have slopes which are somewhat steeper than -1 at most latitudes and altitudes (Liu, 2019). Although our current focus is not on the model or spectral slopes of VMFs, but on Aeolus effects, we have an opportunity to discuss also the spectral slopes for various wave species that has not been done before for the ECMWF system.

4.3.1 Scale-dependent VMFs in the NoAeolus experiment

The cospectra of the VMFs in the NoAeolus experiment are presented in Fig. 4.10 for the three columns of Table 1, $\overline{\omega' u'_K}$, $\overline{\omega' u'_E}$ and $\overline{\omega' u'_W}$. The Rossby and MRG wave VMFs are not shown due to their complex structure but will be displayed later. The three rows of Fig. 4.10 correspond to the spectra averaged for the whole period, for three months during the QBO disruption at the start of 2020 and for three summer months later in the same year during usual QBO evolution.

The zonally averaged cospectra in the stratosphere are positive (not shown), and upward propagating eastward IG and westward IG have positive and negative cospectra, respectively. However, both eastward-propagating and westward-propagating waves can generally have both positive and negative fluxes at individual wave components and levels, which is the reason for visualizing the absolute values of the cospectra in Fig. 4.10. As seen in later figures, wiggles at large scale are associated with opposite sign of the cospectra at neighbouring wavenumbers.

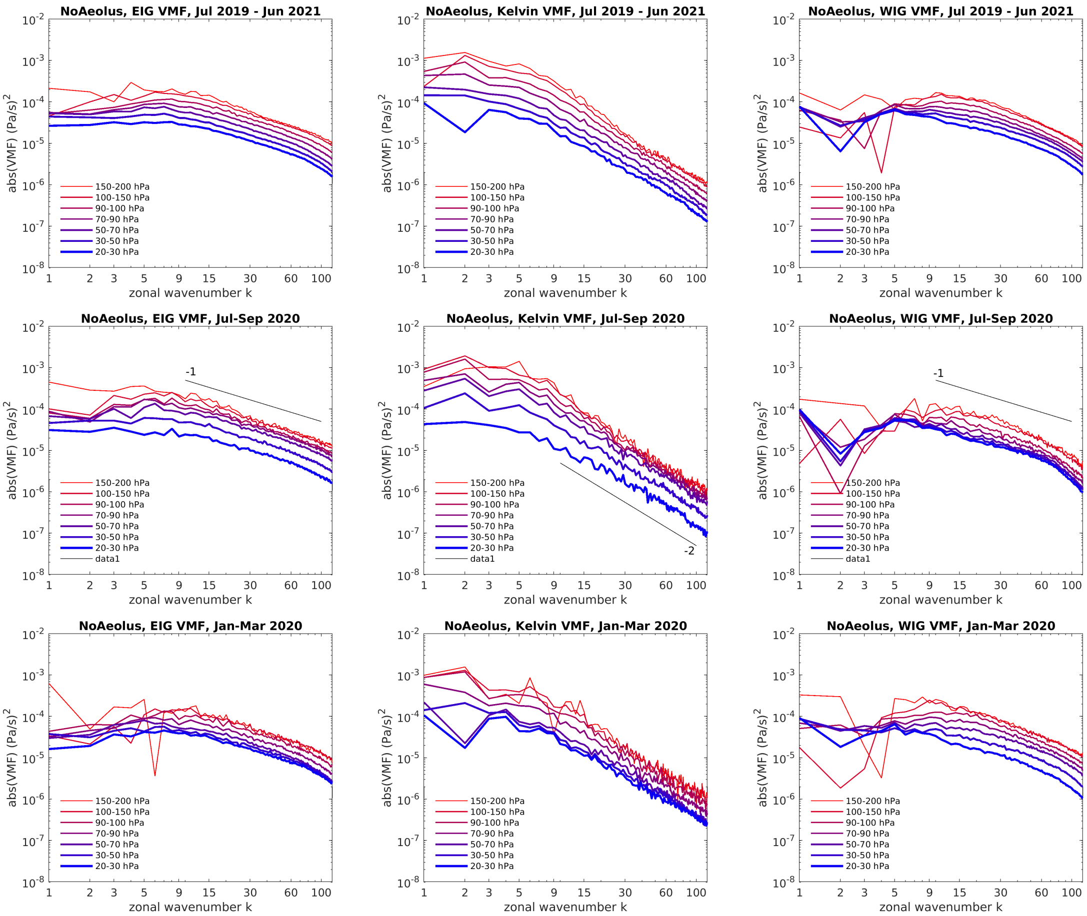

Figure 4.10: Cospectra of the vertical flux of the zonal momentum in the tropics in different layers for and wave species. Left column: EIG waves, center: Kelvin waves, right: WIG waves. Top row: averages for period July 2019-June 2021. Middle row: averages for July-September 2020. Bottom row: averages for January-March 2020.

On average, it is clear from Fig. 4.10 that large scales are dominated by the vertical flux of the Kelvin wave zonal wind. It peaks at $k = 2$ within the TTL. At subsynoptic scales, fluxes of the WIG and EIG waves exceed the Kelvin wave flux for 1-2 orders of magnitude. Their peak scale is around $k = 10$. A different structure of relatively flat stratospheric EIG and WIG cospectra at large scales is likely coupled to the phase of the QBO. This can be seen by comparing the "normal" VMF cospectra during summer 2020 with the spectra during the QBO disruption. During the disruption, fluxes through the stratosphere were enhanced, which is seen in the cospectra for neighbouring layers packed closer together.

4.3.2 Scale analysis of Aeolus effects on VMFs

Now we ask how the assimilation of Aeolus winds affects the cospectra in Fig. 4.10, in particular during the QBO disruption?
Complexity of the VMF diagnostic led us to present stratospheric fluxes level-by-level for different wave species in the NoAeolus experiment along with the differences between Aeolus and NoAeolus OSEs. The upper row in each panel of Fig. 4.11-Fig. 4.12 shows the VMFs for the NoAeolus case and the lower row shows the difference. Three subsequent months during the QBO disruption are shown in Fig. 4.12 and during the normal QBO evolution in Fig. 4.11, the same months as in Fig. 4.10. An important different with Fig. 4.10 is that fluxes are now presented with their signs. The colorbar has been tuned so that positive and negative fluxes can be visualized and that both rows use the same colorbar. This leaves much of mesoscale out of the colour range. However, it has been difficult to interpret differences at small scales as discussed for the vertical velocity.

Profiles of the zonally averaged total VMF show that in normal conditions, the zonally-averaged vertical flux of the zonal momentum is positive and largest at the lowest stratospheric levels (Fig. 4.11, right side profiles). Flux amplitudes and its vertical distribution through the stratosphere depend on the phase of the QBO and season. For example, in Jan 2020 (not shown) the maximal positive flux was near 80 hPa with a value of about 0.6 mPa, and the flux at 100 hPa was negative, which is associated with the background westerlies at 100 hPa supportive for the upward propagation of the WIG waves leading to the negative momentum flux.

The effect of Aeolus, measured by differences in zonally averaged fluxes, is in the zonal average in Fig. 4.11 relatively small, although effects in individual waves can appear large. The largest effect in Fig. 4.11 is in $k = 2$ Rossby wave that may be related to the winter hemisphere (Southern Hemisphere) Rossby waves signals penetrating the tropics near 10°S. The effects are thus sensitive to the latitudinal averaging which is confirmed by comparing results based on averaging between 10°S and 10°N with averaging for the belt 5°S-5°N (not shown).

The VMF differences due to Aeolus depend on the flow. Averaged over 2-year period, largest differences appear at $k = 2$ for the Kelvin and WIG waves and at $k = 1$ for the EIG modes (not shown). Vertical profiles of the zonally-averaged differences typically involve a change of the sign in the VMF difference fields at large scale between 20 hPa and 30 hPa near the zero line of the background wind.

During the QBO disruption (Fig. 4.12), and in particular in January and February

2020, the change of the zonally-averaged VMF profile due to Aeolus exceeds 20% of the flux in the NoAeolus experiment. In addition to the role of the Rossby VMFs at $k = 2$, changes by Aeolus come largely through the eastward-propagating modes, Kelvin and EIG waves, and more so by the Kelvin waves. Changes have the large amplitudes at the largest scales. The change in the sign of the fluxes near 50 hPa can be coupled with the zero line of the wind near this level during the disruption.

Based on amplitudes and signs of the VMF differences, we can conclude that Aeolus enhances the positive VMF by the Kelvin and EIG waves in the layer 100 hPa to 50 hPa, and again above 30 hPa. The $k = 2$ Rossby wave VMF is positive indicating a downward transport of the zonal momentum and the positive difference indicates that Aeolus is increasing the downward Rossby momentum flux at this wavenumber. It is also reducing the upward transport of the Rossby zonal momentum at the neighbouring scales, $k = 1$ and $k = 3$. Changes in the Rossby VMFs also extend higher up in the stratosphere compared to the IG and Kelvin waves. The maximum negative flux near 40 hPa coincides with the location of developing easterlies early in 2020 (Fig. 4.1). Towards summer 2020, the common WQBO phase developed and Aeolus effects diminished, especially in the EIG waves.

In summary, during the 2019/2020 QBO disruption, the assimilation of Aeolus winds in the ECMWF system led to significant changes in stratospheric VMFs averaged for the region 10°away from the equator (up to about 20% at selected wavenumber). This is a large contrast with effects during a typical QBO evolution such as summer 2020 when changes, although large in individual wave species and zonal scales, do not appear as significant in the zonally-averaged fluxes.

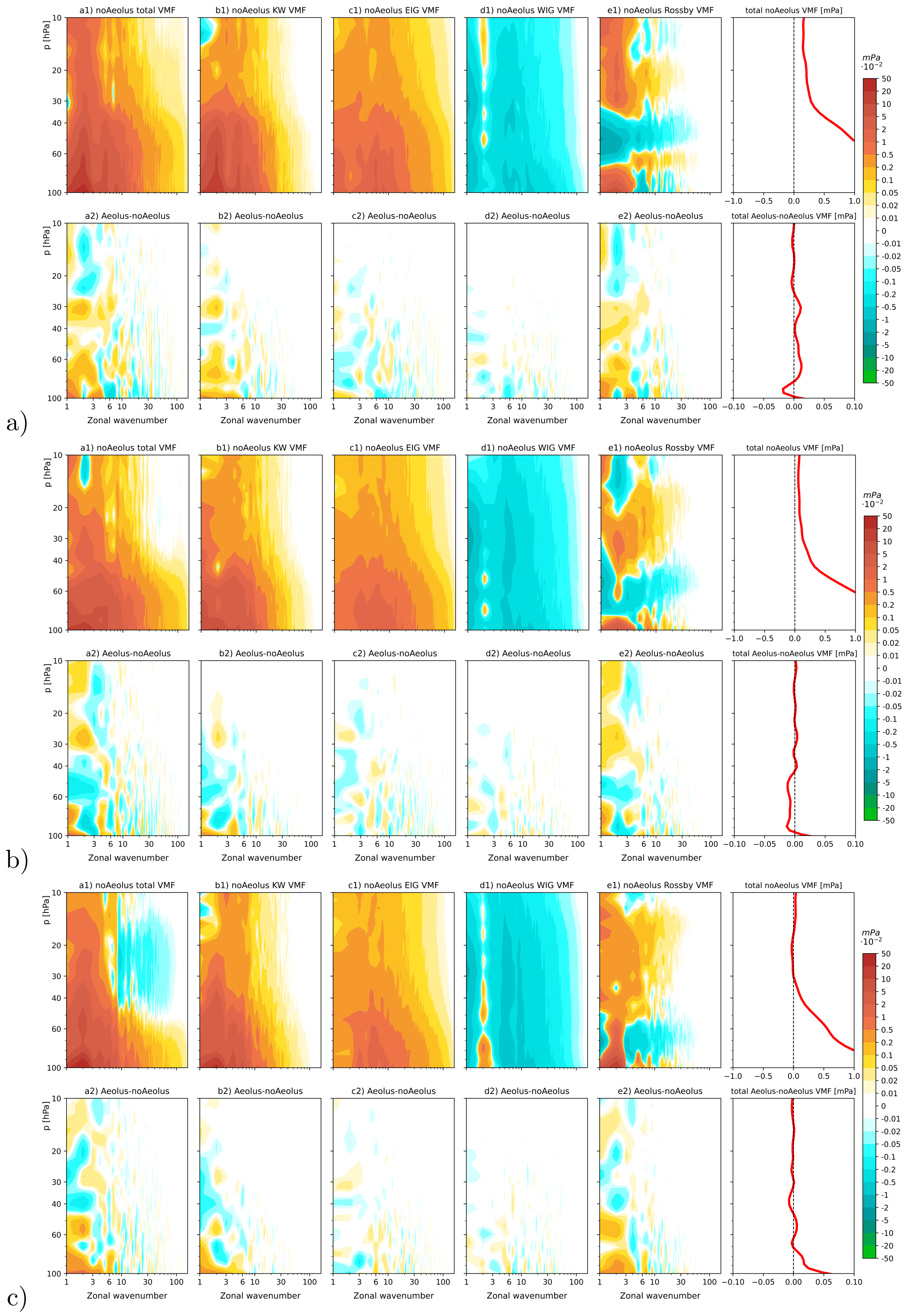

Figure 4.11: Zonal wavenumber cospectra of the vertical flux of the zonal momentum for levels between 100 hPa and 10 hPa in a) July 2020, b) August 2020 and c) September 2020. For each panel, top row shows the VMF cospectra in the NoAeolus experiment for a1) all waves, b1) Kelvin waves, c1) EIG waves, d1) WIG waves and e1) Rossby waves. Bottom row shows Aeolus-NoAeolus for the same wave species. The two panels on the right are the zonally-averaged VMF for (upper) NoAeolus and (lower) Aeolus-NoAeolus.

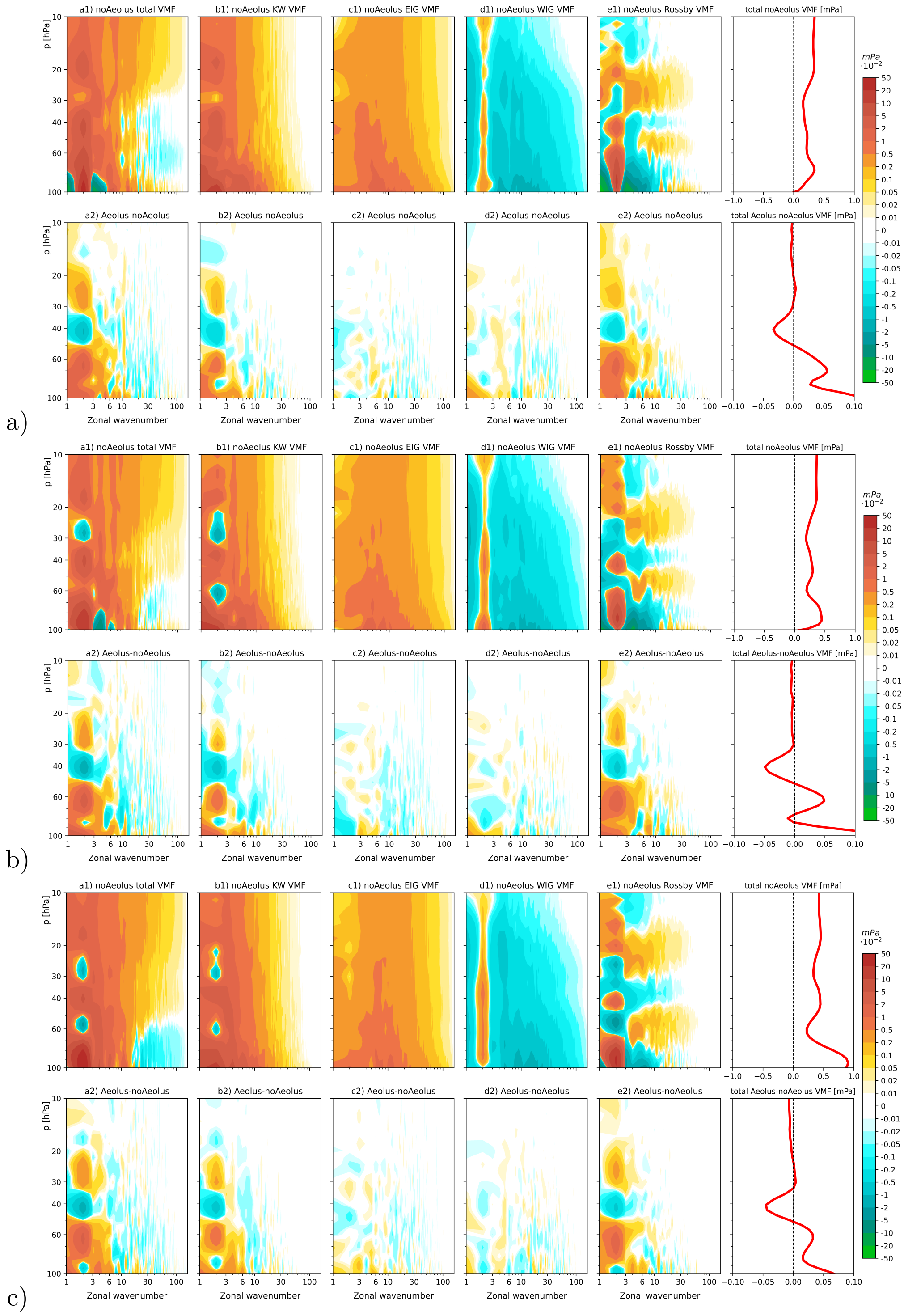

Figure 4.12: As in Fig. 4.11 but for a) January 2020, b) February 2020 and c) March 2020.

Chapter 5

Discussion

We have shown that during the QBO disruption, the assimilation of Aeolus winds produced significant changes in the vertical flux of the zonal momentum, with the strongest effects in the Kelvin wave and Rossby waves, based on the averaging within the belt 10°S−10°S. Now we seek answer to the following question: How are these changes reflected in the stratospheric forecast quality?

Our hypothesis is that a better representation of the vertically-propagating equatorial waves and the related changes in the VMF inevitably lead to better stratospheric forecasts. It is not clear whether and to what extent forecast errors in the stratosphere are associated with large-scale errors in the zonal wind in the TTL due to fast-growing forecast errors in tropical convection. On the other hand, the wave-mean flow interactions due to correction of the mean zonal winds by Aeolus is following by changes in the VMFs. The mean-state stratospheric zonal winds may also be corrected through the thermal wind balance and internal adjustment within 4D-Var with the help of temperature field which is continuously improved by new observations such as COSMIC2 (Healy et al., 2020; Ruston and Healy, 2021b). The changes in the tropical background winds by Aeolus were occurring systematically throughout the OSE period, but they were the largest during the 2019 and 2020 period and particularly large during the QBO disruption.

While not predicted, the disruption was observed *in situ* and therefore the mean zonal winds were corrected. In Chapter 4 we discussed that changes in the mean state by Aeolus altered the VMFs during the disruption in Dec 2019-Jan 2020. In normal QBO conditions such as summer 2020, it was the vertical gradient of the VMF (wave drag) that was driving the changes in the background flow. The two different mechanism of the Aeolus impact in the stratosphere raise the question of variations in the forecast quality during the OSE period.

Our original hypothesis was that the forecast improvements will be coupled with ability of the vertically-propagating waves coupled to convection, especially the Kelvin waves, to reach higher levels in the stratosphere and through the wave-mean flow interactions improve the forecasts of the mean flow. Favourable conditions are thus mean easterlies in the lower stratosphere such as in the first part of 2020 following the disruption. Impact of Aeolus during an extreme event such as the QBO disruption likely depends both on observing the zonal-mean zonal wind and on providing better initial conditions for the tropospheric wave forcing of the event progression.

Usually, forecast verification of Aeolus is performed for the complete study period. It is not possible to account for flow dependency of forecast errors on low-frequency variability such as the ENSO. Nevertheless with everything else the same but Aeolus data assimilation, it is meaningful to investigate variations in forecast quality during the OSE. Therefore we carried out verification of the winds and temperature forecast during the OSE at different pressure levels.

The impact of Aeolus winds on stratospheric zonal wind forecasts is presented in Fig. 5.1 for the tropical belt 20°S-20°N amd 100 hPa level. The difference in root-mean-square errors (rmse) in Aeolus and NoAeolus experiments compared to analyses is normalized by the NoAeolus experiment rmse in 1.5-month bins starting with 1 July 2019. A relative improvement in the Aeolus experiment compared to NoAeolus is shown as negative values of the normalized rmse. The vertical bars in Fig. 5.1 denote 95% confidence interval and are used to quantify statistically significant results as period with vertical bars below the zero line.

Figure 5.1 shows that changes at 100 hPa varied from positive and statistically significant forecast improvement by Aeolus only after forecast day 3 in summer 2019 to 4-5% forecast improvement from the start of forecasts in January 2020 (Fig. 5.1e). Similarly positive effects but with a smaller magnitude are found till the end of the OSE in June 2021 (Fig. 5.1f-o). Based on the results of Chapter 4, we suggest that the largest improvements in January 2020 were due to observing the mean zonal winds affected by the extreme event of extratropical origin.

If forecast improvements are driven by wave forcing, then positive impacts at 100 hPa should be associated with similar or greater positive effects higher up. This can be verified in Fig. 5.2. It shows that from January to March 2020, forecast improvements at 70 hPa level were in the range 15-20% were for forecast day 1. At 50 hPa, the day 1 forecast improvements were 8-10% diminishing to 2-4% at 20 hPa. Here we expect, based on the results in Chapter 4, that large improvements come from improved wave forcing by Aeolus as well as correction of the mean state. To quantify the positive effects on wave propagation versus effects on the mean flow, a further analysis of forecast quality for individual wave types is planned.

In the second part of the period, July 2020 to June 2021, the impact of Aeolus at these higher levels was slightly positive but the results are not statistically significant beyond day 1, and the scores are not shown.

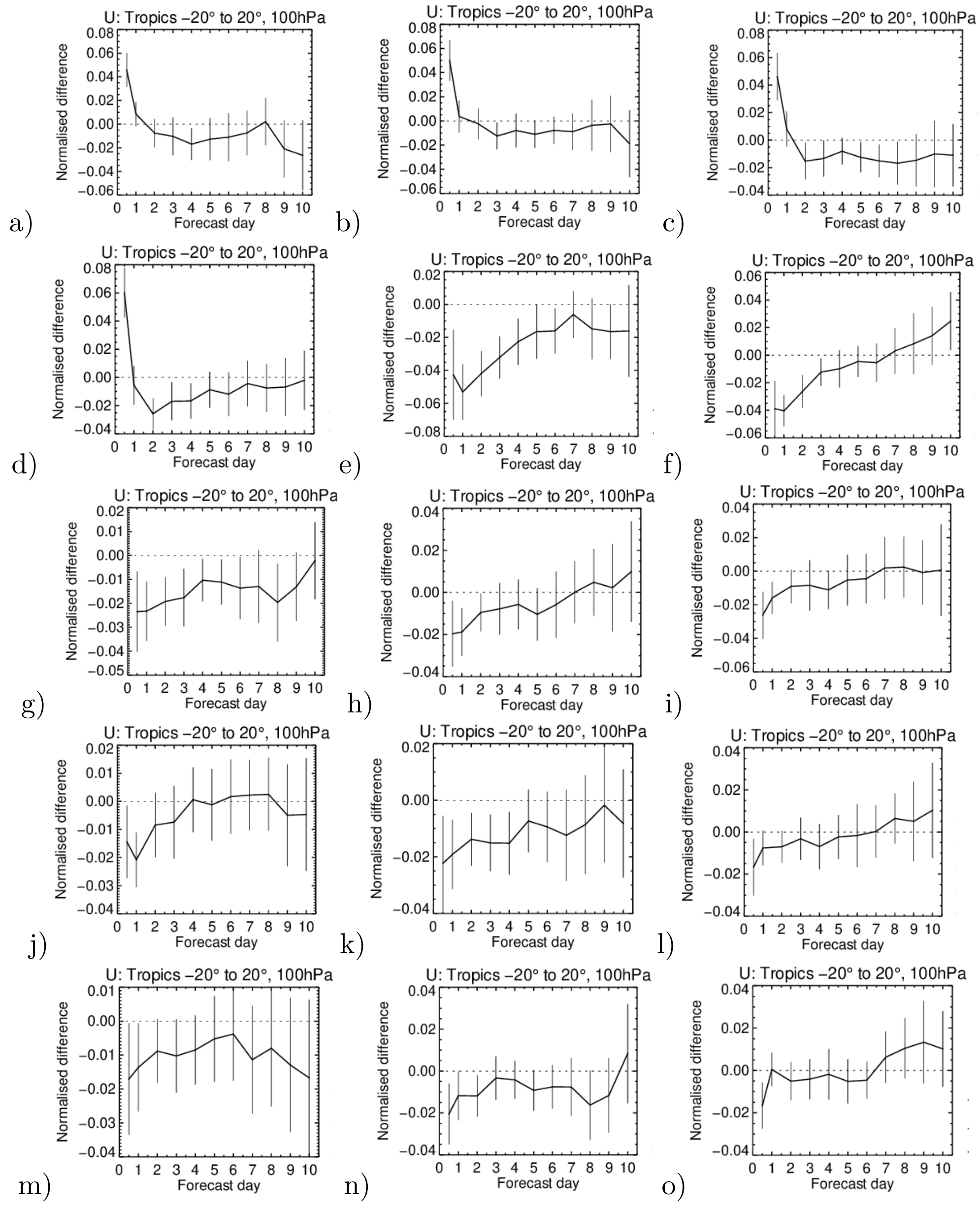

Figure 5.1: Normalized difference of the root-mean-square errors (rmse) of forecasts minus respective analyses for zonal winds in the tropics at 100 hPa. The difference is taken between the rmse of Aeolus and NoAeolus experiments and the normalization is by the rmse of the NoAeolus experiment. The error bars for 95% confidence intervals are included. The rmse are computed for subsequent 1.5 month long periods. a) 1 Jul-15 Aug 2019, b) 16 Aug-30 Sep 2019, c) 1 Oct-15 Nov 2019, d) 16 Nov-31 Dec 2019, e) 1 Jan-15 Feb 2020, f) 16 Feb-31 Mar 2020, g) 1 Apr-15 May 2020, h) 16 May-30 Jun, i) 1 Jul-15 Aug 2020, j) 16 Aug-30 Sep 2020, k) 1 Oct -15 Nov 2020, l) 16 Nov-31 Dec 2020, m) 1 Jan-15 Feb 2021, n) 16 Feb-31 Mar 2021 and o) 1 Apr-15 May 2021.

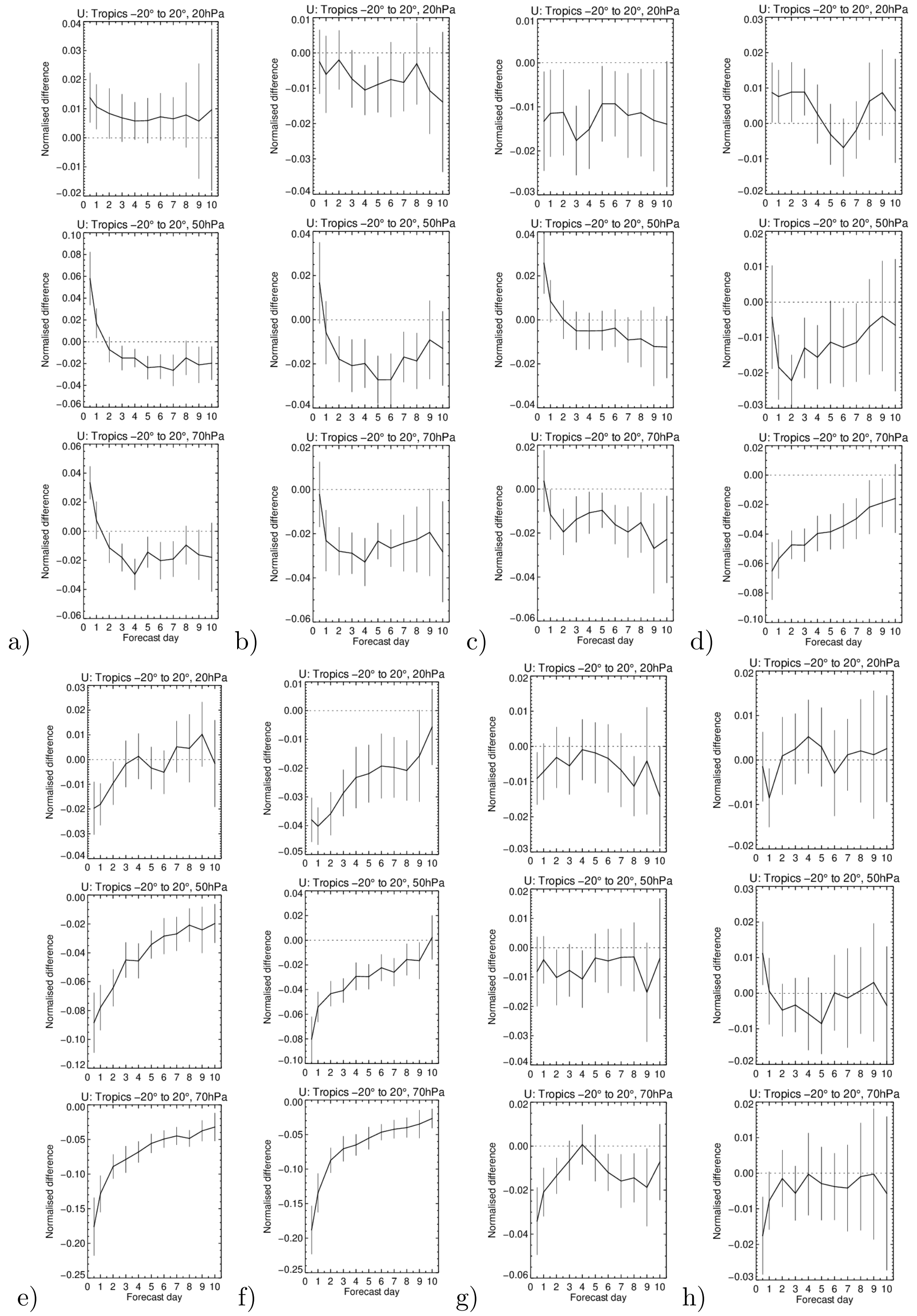

Figure 5.2: As in Fig. 5.1 but for the levels 20 hPa (top row in every panel), 50 hPa (middle row in every panel) and 70 hPa (bottom row in every panel). a) 1 Jul-15 Aug 2019, b) 16 Aug-30 Sep 2019, c) 1 Oct-15 Nov 2019, d) 16 Nov-31 Dec 2019, e) 1 Jan-15 Feb 2020, f) 16 Feb-31 Mar 2020, g) 1 Apr-15 May 2020 and h) 16 May-30 Jun.

Chapter 6

Summary, conclusions and recommendations

We analysed two derived quantities, the vertical velocity and vertical momentum fluxes, in the ECMWF Observing System Experiments with the 2nd preprocessed FM-B Aeolus winds. The vertical velocity transports moisture upward and thereby drives the global hydrological cycle. Much of it takes place in the tropics. Equatorial waves coupled to convection propagate vertically from the upper troposphere into the stratosphere, break and dissipate throughout the stratosphere depending on the background flow, and deposit momentum which drives stratospheric variability such as the quasi-biennial oscillation. While the two-year OSE is the longest such experiment available, it is not long enough for a detailed study of the QBO. But, it is long enough to quantify Aeolus effects on equatorial Kelvin, Rossby, mixed Rossby-gravity, and eastward- and westward-propagating inertia-gravity waves propagating in shear flows. Moreover, the study period includes the QBO disruption offering a unique opportunity to investigate the value of wind profile observations for analyses and forecasts of a global-scale extreme event. That value is a highlight of this report and is shown also in the executive summary.

The work package 1 of the project and the first technical note showed that the assimilation of Aeolus winds enhanced amplitudes of large-scale equatorial waves and enhanced the vertical shear of the zonal wind in the tropical tropopause layer. By doing this, Aeolus might have not only provided missing wind information but also corrected model errors such as the representation of vertical diffusion. At small scales, Aeolus data was shown to systematically reduce amplitudes of signals projecting on the inertia-gravity modes i.e. divergent circulation that also may be related to model and data assimilation properties. While a better understanding of coupling between effects of Aeolus and formulation of the ECMWF data assimilation system is a subject of the Work Package 5, the Work Package 2 presented in this report investigates Aeolus effects on the vertical velocity and the vertical momentum fluxes in relation to the background flow in the stratosphere.

The main findings are summarized in the following three paragraphs, each answering one of the questions addressed by the work package.

1. What are the effects of Aeolus winds on the vertical velocity in the tropical UTLS

region?

The scale-dependent effects of Aeolus on vertical velocity are results of Aeolus's effects on divergence across a large range of subsynoptic scales. Analyses with Aeolus winds have systematically weaker updrafts and downdrafts associated with IG waves, especially in the upper troposphere. This is due to a systematic reduction of the amplitude of the divergent horizontal winds throughout the UTLS, as reported in TN1. The spectrum of mean-square differences (MSD) of Aeolus-NoAeolus vertical motions shows the largest MSD in the inertia-gravity (IG, or divergent modes) near the zonal wavenumber $k = 80$. At large scales, significant effects of Aeolus were found only in the Kelvin wave vertical velocity with the strongest effect (around 5%) in $k = 3 - 5$ during and following the QBO disruption.

2. How does Aeolus winds affect the vertical flux of the horizontal momentum in the tropics?

   The assimilation of Aeolus winds produces differences in the vertical momentum fluxes primarily by changing the horizontal wind perturbations associated with various equatorial waves species. When measured by differences in zonally averaged fluxes within 10°S and 10°N, the effects are relatively small (below 1%). However, effects in individual scales of various waves can be large depending on the background flow. In early 2020, the period of the QBO disruption, the assimilation of Aeolus winds in the ECMWF system resulted in up to about 20% change in stratospheric VMFs. The most affected wave was the Kelvin wave ($k = 2$) in the easterly background flow in the lower stratosphere in 2020.

   Aeolus affects stratospheric wave-mean flow interactions in two ways. First, Aeolus corrects background zonal winds, with aligned changes in the VMFs, such as during the QBO disruption in the lower stratosphere. In normal QBO conditions such as summer 2020, the change of the vertical gradient of the VMFs, which represents wave forcing, is aligned with the changes in the background flow due to Aeolus winds. In this way, Aeolus winds improve the transition between the two phases of the QBO.

3. How does the Aeolus impact on tropical wave activity influence stratospheric forecasts?

   Quality of stratospheric forecasts largely varied during the first year of the OSE and especially during the QBO disruption. Forecast improvements of a few % with respect to NoAEolus near the tropical tropopause increased to about 15% improvements in day 1 forecasts in the lower stratosphere early in 2020 as Aeolus corrected zonal winds and associated vertical shear during the extreme event of extratropical origin - the QBO disruption.

The results were produced by a novel methodology of analysing tropical wave activity applied to the two-year long analysis dataset between July 2019 and June 2021. Extending results to the FM-A dataset covering the first part of Aeolus life before July 2019, which was recently completed at the ECMWF, and to the period after July 2021 till the end of Aeolus life, would make possible a more detailed analysis of forecast scores in relation to the flow. Dominance of low-frequency variability in the studied period by the QBO disruption, along with a continued degradation of the quality of HLOS winds and the introduction of other observing systems such as COSMIC2, prevents us from making conclusions about Aeolus effects on subseasonal variability such as the Madden-Julian Oscillation. Nevertheless, the work will continue on studying coupling between Aeolus data and wave activity in the UTLS, especially on the complementary roles of the Aeolus winds and COSMIC2 temperature profiles.

Based on the presented results and expectations from Aeolus follow-on missions, we recommend several potential activities by the Aeolus follow-on (or Aeolus2) missions:

1. Effects of Aeolus winds on the vertical momentum fluxes driving the QBO and stratospheric variability suggest that Aeolus follow-on missions are likely to contribute to extratropical predictability via the so-called stratospheric path. In preparation for Aeolus2, observing system simulation experiments should include extended-range forecasts that can show whether such effect i.e. extension of practical predictability can be expected.

2. Effects of Aeolus winds on the vertical velocity, along with effects on the horizontal wind divergence at subsynoptic scales discussed in TN1, suggest that Aeolus2 will be a key information source about mesoscale winds. This information is much less likely obtainable through advanced data assimilation scheme, in contrast to large scales. We thus suggest to study effects of Aeolus2 on extratropical mesoscale processes with significant vertical velocities such as fronts and mesoscale instabilities, an well as to extend the current study to smaller spatial scales and convective processes in the tropics, especially in the inter-tropical convergence zone.

3. The method and results of this work can be relevant for the ESA's EarthCARE mission that has as one of its goals observations of characteristics of vertical motions within clouds[3]. It may be related to the vertical velocity analysis carried out in this project and provide additional coupling the EarthCARE Aeolus missions. Theory-based cross-comparison can be carried out with the profiles of radiative heating and cooling from EarthCARE and ECMWF system and diabatic forcing from other observing systems and the ECMWF analyses and forecasts.

[3]https://www.esa.int/Applications/Observing_the_Earth/FutureEO/EarthCARE/EarthCARE_goals

Bibliography

Andrews, D. G., J. R. Holton, and C. B. Leovy, 1987: *Middle atmosphere dynamics.* Academic Press, Inc.

Anstey, J., T. Banyard, N. Butchart, L. Coy, P. Newman, S. Osprey, and C. Wright, 2021: Prospect of increased disruption to the QBO in a changing climate. *Geophy. Res. Lett.* **48**, e2021GL093058.

Baldwin, M. P., L. J. Gray, T. J. Dunkerton, K. Hamilton, P. H. Haynes, W. J. Randel, J. R. Holton, M. J. Alexander, I. Hirota, T. Horinouchi, D. B. A. Jones, J. S. Kinnersley, C. Marquardt, K. Sato, and M. Takahashi, 2001: The quasi-biennial oscillation. *Rev. Geophys.* **39**, 179–229.

Banyard, T. P., C. J. Wright, S. M. Osprey, N. P. Hindley, G. Halloran, L. Coy, P. A. Newman, N. Butchart, M. Bramberger, and M. J. Alexander, 2024: Aeolus wind lidar observations of the 2019/2020 quasi-biennial oscillation disruption with comparison to radiosondes and reanalysis. *Atmospheric Chemistry and Physics* **24**(4), 2465–2490.

Bormann, N., L. Magnusson, D. Duncan, and M. Dahoui, 2023: Characterisation and correction of orbital biases in AMSU-A and ATMS observations in the ECMWF system.

De Chiara, G., L. Magnusson, M. Rennie, S. Abdalla, and S. Healy, 2023: The Contribution of Aeolus to the Prediction of Extreme Weather Events Contract Report to the European Space Agency, ESA ESTEC contract No. 4000134449/20/NL/FF/tfd, Ref: AE-TN-ECMWF-GS-175, Version 1.2 of 16 June 2023, 76 pages.

Dörnbrack, A., S. Gisinger, N. Kaifler, T. Portele, M. Bramberger, M. Rapp, M. Gerding, J. Söder, N. Žagar, and D. Jelić, 2018: Gravity waves excited during a minor sudden stratospheric warming. *Atmos. Chem. Phy.* **18**(17), 12915–12931.

Fritts, D. C. and J. M. Alexander, 2003: Gravity wave dynamics and effects in the middle atmosphere. *Reviews of Geophysics* **41**(1), doi:10.1029/2001RG000106.

Healy, S., I. Polichtchouk, and A. Horányi, 2020: Monthly and zonally averaged zonal wind information in the equatorial stratosphere provided by GNSS radio occultation. *Q. J. R. Meteorol. Soc.* **146**(732), 3612–3621.

Kang, M.-J. and H.-Y. Chun, 2021: Contributions of equatorial waves and small-scale convective gravity waves to the 2019/20 quasi-biennial oscillation (QBO) disruption. *Atmospheric Chemistry and Physics* **21**(12), 9839–9857.

Kang, M.-J., H.-Y. Chun, and R. R. Garcia, 2020: Role of equatorial waves and convective gravity waves in the 2015/16 quasi-biennial oscillation disruption. *Atmospheric Chemistry and Physics* **20**(23), 14669–14693.

Kim, Y.-H. and H.-Y. Chun, 2015a: Contributions of equatorial wave modes and parameterized gravity waves to the tropical QBO in HadGEM2. *Journal of Geophysical Research: Atmospheres* **120**(3), 1065–1090.

Kim, Y.-H. and H.-Y. Chun, 2015b: Momentum forcing of the quasi-biennial oscillation by equatorial waves in recent reanalyses. *Atmospheric Chemistry and Physics* **15**(12), 6577–6587.

Liu, H., 2019: Quantifying gravity wave forcing using scale invariance. *Nat. Commun.* **10**, 2605.

Martin, A., M. Weissmann, and A. Cress, 2023: Investigation of links between dynamical scenarios and particularly high impact of Aeolus on numerical weather prediction (NWP) forecasts. *Weather and Climate Dynamics* **4**(1), 249–264.

Nappo, C., 2002: *An introduction to atmospheric gravity waves.* Amsterdam: Academic Press, 2002 International geophysics series, vol. 85, ISBN 0125140827.

Neduhal, V., N. Žagar, F. Lunkeit, I. Polichtchouk, and Ž. Zaplotnik, 2023: Decomposition of the horizontal wind divergence associated with the Rossby, inertia-gravity, mixed Rossby-gravity and Kelvin waves on the sphere. *J. Geophy. Res.-Atmosphere*, submitted.

Plougonven, R., A. de la Cámara, A. Hertzog, and F. Lott, 2020: How does knowledge of atmospheric gravity waves guide their parameterizations? *Q. J. R. Meteorol. Soc.* **146**(728), 1529–1543.

Polichtchouk, I., N. Wedi, and Y.-H. Kim, 2022: Resolved gravity waves in the tropical stratosphere: Impact of horizontal resolution and deep convection parametrization. *Q. J. R. Meteorol. Soc.* **148**, 233–251.

Raphaldini, B., T. Wakate, S. Andre, P. S. Dias, V. C. Mayta, and V. Takara, 2020: Normal Mode Perspective on the 2016 QBO Disruption: Evidence for a Basic State Regime Transition. *Geophy. Res. Lett.* **487**(14), e2020GL087274.

Rennie, M. and L. Isaksen, 2024: The NWP impact of Aeolus Level-2B winds at ECMWF. ESA Contract Report, Aeolus DISC contract No. 4000126336/18/I-BG, WP-5500, 284 pages. Available from https://www.ecmwf.int/en/elibrary/81546-nwp-impact-aeolus-level-2b-winds-ecmwf.

Rennie, M. P., L. Isaksen, F. Weiler, J. de Kloe, T. Kanitz, and O. Reitebuch, 2021: The impact of Aeolus wind retrievals on ECMWF global weather forecasts. *Quarterly Journal of the Royal Meteorological Society* **147**(740), 3555–3586.

Richter, J., J. Anstey, N. Butchart, Y. Kawatani, G. Meehl, S. Osprey, and I. Simpson, 2020: Progress in Simulating the Quasi-Biennial Oscillation in CMIP Models. *Journal of Geophysical Research: Atmospheres* **125**(8), e2019JD032362.

Richter, J., N. Butchart, Y. Kawatani, A. Bushell, L. Holt, F. Serva, J. Anstey, I. Simpson, S. Osprey, K. Hamilton, P. Braesicke, C. Cagnazzo, C.-C. Chen, R. Garcia, L. Gray, T. Kerzenmacher, F. Lott, C. McLandress, H. Naoe, J. Scinocca, T. Stockdale, S. Versick, S. Watanabe, K. Yoshida, and S. Yukimoto, 2022: Response of the quasi-biennial oscillation to a warming climate in global climate models. *Quarterly Journal of the Royal Meteorological Society* **148**(744), 1490–1518.

Ruston, B. and S. Healy, 2021a: Forecast Impact of FORMOSAT-7/COSMIC-2 GNSS Radio Occultation Measurements. *Atmospheric Science Letters* **22**(3), e1019.

Ruston, B. and S. Healy, 2021b: Forecast Impact of FORMOSAT-7/COSMIC-2 GNSS Radio Occultation Measurements. *Atmos. Sci. Lett.* **22**, 22:e1019.

Scaife, A. A., M. A. and. M Andrews, A. Arribas, M. Baldwin, and N. D. et al., 2014: Predictability of the quasi-biennial oscillation and its northern winter teleconnection on seasonal to decadal timescales. *Geophy. Res. Lett.* **41**, 1752–1758.

Schreiner, W., J. Weiss, R. Anthes, J. Braun, V. Chu, J. Fong, D. Hunt, Y.-H. Kuo, T. Meehan, W. Serafino, J. Sjoberg, S. Sokolovskiy, E. Talaat, T. Wee, and Z. Zeng, 2020: COSMIC-2 Radio Occultation Constellation: First Results. *Geophysical Research Letters* **47**(4), e2019GL086841.

Simmons, A. and D. Burridge, 1981: An Energy and Angular-Momentum Conserving Vertical Finite-Difference Scheme and Hybrid Vertical Coordinates. *Mon. Wea. Rev.* **109**, 758 – 766.

Wheeler, M. and G. N. Kiladis, 1999: Convectively coupled equatorial waves: analysis of clouds and temperature in the wavenumber-frequency domain. *J. Atmos. Sci.* **56**, 374–399.

Žagar, N., A. Kasahara, K. Terasaki, J. Tribbia, and H. Tanaka, 2015: Normal-mode function representation of global 3D datasets: open-access software for the atmospheric research community. *Geosci. Model Dev.* **8**, 1169–1195.

Žagar, N., V. Neduhal, S. Vasylkevych, Ž. Zaplotnik, and H. Tanaka, 2023: Decomposition of vertical velocity and its zonal wavenumber kinetic energy spectra in the hydrostatic atmosphere. *J. Atmos. Sci.* **80**, 2747–2767.

Žagar, N. and J. Tribbia, 2020: *Modal View Of Atmospheric Variability: Applications Of Normal-Mode Function Decomposition in Weather and Climate Research.* Springer Nature.

Žagar, N., J. Tribbia, J. L. Anderson, and K. Raeder, 2011: Balance of the background-error variances in the ensemble assimilation system DART/CAM. *Mon. Wea. Rev.* **139**, 2061–2079.

Acronyms and Glossary

Table 6.1: List of acronyms and their definitions

Acronym	Definition
3D	Three-dimensional
4D-Var	Four-dimensional variational data assimilation
COSMIC2	Constellation Observing System for Meteorology Ionosphere and Climate - 2
ECMWF	European Centre for Medium-Range Weather Forecasts
EIG	Eastward Inertia-Gravity wave
ERA-Interim	ECMWF Reanalysis system preceding the ERA5
ERA5	ECMWF Reanalysis v5
ESA	European Space Agency
FM-B	Flight model B
GNSS-RO	Global Navigation Satellite System Radio Occultation
HLOS	Horizontal line-of-sight
IFS	Integrated Forecasting System (at ECMWF)
IG	Inertia-Gravity wave
KW	Kelvin wave
L1B	Level 1B
L2B	Level 2B
MARS	Meteorological Archival and Retrieval System
MRG	Mixed Rossby-Gravity wave
MSD	Mean squared difference
n1Rossby	$n = 1$ Rossby wave
NH	Northern Hemisphere
NWP	Numerical weather prediction
OSE	Observing system experiment
QBO	Quasi-biennial oscillation
RMSD	Root mean squared difference
RMSE	Root mean squared error
SH	Southern Hemisphere
TN	Technical note
TTL	Tropical tropopause layer
U	Zonal wind
UTLS	Upper troposphere - lower stratosphere
V	Meridional wind
VKE	Vertical kinetic energy
VMF	Vertical momentum flux
WIG	Westward Inertia-Gravity wave
WP	Work Package

Glossary of the main terms

4D-Var – Three-dimensional variational data assimilation performs objective analysis of the atmospheric state within a given time window by minimizing the so-called cost function, which is the sum of the squares of distances of the optimal analysis state from the observations and from the background field (a short-term forecast), each weighted by their error variances. The evaluation of the cost function involves the observation operator H which transform the model prognostic variables into observed quantities at their observational locations. In the case of Aeolus, H involves the computation of the horizontal line-of-sight wind from the zonal and meridional wind components from the model. In contrast to 3D-Var, which does not involve the evolution of the model, 4D-Var requires a linearized version of the forecast model and its adjoint to constrain the analysis solution in time.

COSMIC2 (or COSMIC-2) – The constellation of satellites launched in June 2019 with full operational capability achieved in October 2021. Using Global Navigation Satellite System (GNSS) Radio Occultation to measure changes in the relative position with respect to the GNSS satellite COSMIC2 provides vertical scanning of the atmosphere, as the signal received from the GNSS satellite passes through the atmosphere and gets refracted along the way. The magnitude of the refraction depends on the temperature and water vapor concentration in the atmosphere.

Inertia-gravity waves – Internal waves propagating through the atmosphere (or ocean) under the influence of the buoyancy and Coriolis forces. If the Coriolis force can be neglected, one refers to gravity waves. Together with Rossby waves, Kelvin waves and mixed Rossby-gravity waves, inertia-gravity (IG) waves constitute the eigensolutions of the linearized primitive equations of atmospheric motions. IG waves have frequencies in the range between N, the buoyancy frequency, and f, the inertial frequency, which is also the Coriolis parameter. The group velocity of IG waves is perpendicular to their phase velocity meaning that for the vertical energy propagation the IG wave group velocity is upward whereas their phase velocity is downward.

Kelvin wave – Atmospheric Kelvin wave is one of eigensolutions of the linearized primitive equations. It arises as a special solution of on the equatorial $\beta-$plane, on the sphere or in the channel with walls. In the tropical atmosphere, the maximal zonal velocity and height perturbations of the wave are on the equator, and are in geostrophic balance. The wave height decreases exponentially from the equator with an e-folding length scale equal known as the equatorial deformation radius. In the shallow-water approximation, the Kelvin wave is non-dispersive with phase speed equal to the phase speed of surface gravity wave in the case of no rotation. As the slowest eastward-propagating eigenmode of the global atmosphere, Kelvin wave is a part of the response to any forcing and is widely studied in weather and climate research.

Mixed Rossby-gravity wave (or Yanai wave) – Atmospheric mixed Rossby-gravity

(MRG) wave is a special solution of the linearized primitive equations on the equatorial $\beta-$plane or on the sphere. MRG wave has a meridional velocity component symmetrical about the equator with the maximal value at the equator. Its zonal velocity component and geopotential height perturbations are asymmetrical about the equator and approximately coupled geostrophically. As its name says, the MRG wave has properties of the Rossby wave that become stronger as the zonal wavenumber increases, and of the gravity wave. The phase speed of MRG waves is westward and they are faster than Rossby waves but slower than any IG wave. Together with the Kelvin wave, MRG wave fills the frequency gaps between the Rossby and IG wave present in midlatitude. In the tropics, MRG waves are excited by every forcing that is asymmetrical about the equator as well as dynamical processes.

MODES software – MODES applies three-dimensional linear wave theory for the decomposition of atmospheric circulation on the sphere. MODES outputs quantify spatial and temporal variability associated with the two main circulation regimes, the Rossby wave (or balanced) regime and the inertia-gravity wave (or unbalanced) regime. The approach is most useful in the tropics where the two special NMF solutions, the Kelvin wave and the mixed Rossby-gravity wave, account for a significant part of tropical variability. The software is available via the MODES webpage, `https://modes.cen.uni-hamburg.de`, that also provides real-time results of the decomposition of the operational deterministic ECMWF 10-day forecasts, as well as selected outputs of modal analysis, theoretical solutions and references.

$n = 1$ **Rossby wave** – This is the gravest among the Rossby waves on the sphere and the leading westward-propagating balanced eigensolution of the linearized primitive equations on the sphere or on the equatorial $\beta-$plane. For Rossby waves on the sphere, index n corresponds to the Hough function index, where Hough function describe the meridional structure of eigensolutions. The zonal structure is that of waves. The wave with $n = 1$ is the fastest Rossby wave on the sphere and one of the few eigensolutions detected in observations, along with the Kelvin and MRG waves. It is a part of the so-called Matsuno-Gill solution of the tropical circulation in response to heating, and is believed to be a part of the response associated with the Madden-Julian Oscillation, among others. The horizontal structure of the $n = 1$ Rossby wave for different background fluid depths can be seen at `https://modes.cen.uni-hamburg.de/Hough#part2_2`, along with other waves discussed in the TN.

Observing System Experiment (OSE) – An OSE experiment is carried out to understand and quantify the impact of existing observing system, such as Aeolus, on the initial state (analysis) and forecasts. If OSE is carried out for the impact of future observations, it is called OSSE, i.e. Observing System Simulation Experiment. Every OSE requires two experiments; the referent or control experiment which makes use of all data except the data which one wants to evaluate, and a sensitivity experiment with observations of interest added on top of all other data. The OSE results are evaluated by comparing the sensitivity experiment with the control experiment by possibly by comparing both experiments with the third experiment (e.g. operational system).

Quasi-biennial oscillation (QBO) – The QBO is an oscillation in the zonal winds of the equatorial stratosphere with a period that fluctuates between about 25 and 30 months. This is manifested as a downward propagation of easterly or westerly winds starting near the top of the lower stratosphere (10 hPa) and propagating downwards at about 1 km per month speed towards the tropopause. The easterly phase winds are about twice as stronger than the westerly phase. The QBO is commonly described by the monthly mean, zonal mean wind in the belt 5°or 10° about the equator. As an QBO index one often uses winds at 30 hPa from sonde data. The mechanism behind the QBO are waves emanating from the tropical troposphere including the Kelvin wave, mixed Rossby-gravity waves and a spectrum of IG waves. The exact role of various waves in driving the QBO remains unclear as well as its role on the tropospheric processes and global predictability. The QBO remains a challenge for the climate models to simulate.

Rossby waves – Rossby waves are the main building block of atmospheric motions in extratropics on day-to-day scales. Theoretically, the barotropic Rossby wave is defined as a wave on a uniform current in a two-dimensional rotating fluid on the $\beta-$plane that is a local approximation of the sphere accounting for the variability of the Coriolis parameter. The barotropic Rossby wave conserve absolute vorticity. In the stratified atmosphere, baroclinic Rossby waves conserve the potential vorticity. Rossby waves move westward relative to the background flow, but on weather maps appear effectively moving eastward as they are advected by the mean westerly winds. Derived from eigensolution of the linearized primitive equations on the sphere, Rossby waves are defined by the zonal wavenumber, meridional mode index denoted n, and the vertical structure. Global data assimilation system for weather prediction aim at accurate prediction of the Rossby wave variability in medium-range forecasts.

Tropical upper troposphere and lower stratosphere (UTLS) – The UTLS region in the tropical atmosphere includes the tropical tropopause layer (TTL) and is a transition region between the stratosphere and the troposphere in which the air has mixed stratospheric and tropospheric properties. Within the UTLS there are large changes in the ozone, temperature large lapse rates and radiative heating that shape the heat, moisture and chemistry budgets. In particular, deep moist tropospheric convection generates a spectrum of waves that propagate vertically and affect the circulation in the lower stratosphere and above. It is believed that this process is one way how tropical processes affect extratropical circulation and its extended predictability.